JOURNAL OF GEOPHYSICAL RESEARCH, VOL. 99, NO. E12, PAGES 25,959–25,991, DECEMBER 25, 1994

Thermal and albedo mapping of the polar regions of Mars using Viking thermal mapper observations
1. North polar region

David A. Paige, Jennifer E. Bachman, and Kenneth D. Keegan
Department of Earth and Space Sciences, University of California, Los Angeles

Abstract. We present the first maps of the apparent thermal inertia and albedo of the north polar region of Mars. The observations used to create these maps were acquired by the infrared thermal mapper (IRTM) instruments on the two Viking orbiters over a 50-day period in 1978 during the Martian early northern summer season. The maps cover the region from 60°N to the north pole at a spatial resolution of 1/2° of latitude. The analysis and interpretation of these maps is aided by the results of a one-dimensional radiative convective model, which is used to calculate diurnal variations in surface and atmospheric temperatures, and brightness temperatures at the top of the atmosphere for a wide range of assumptions concerning aerosol optical properties and aerosol optical depths. The results of these calculations show that the effects of the Martian atmosphere on remote determinations of surface thermal inertia are more significant than have been indicated in previous studies. The maps of apparent thermal inertia and albedo show a great deal of spatial structure that is well correlated with surface features. The north residual polar cap has a very high apparent thermal inertia, and is interpreted to contain dense, coarse-grained, or solid water ice that extends from within 2 mm of the surface to depths of at least 1 m below the surface. Detached, bright water ice deposits surrounding the residual cap also have very high apparent thermal inertias, and are interpreted to have similar properties. Polar layered deposits surrounding the north residual cap also have high apparent thermal inertias, and are also interpreted to contain near-surface water ice. Mariner 9 images of the north residual cap obtained in 1972 show much less bright water frost coverage than Viking images obtained three Mars years later in 1978, and it is suggested that layered deposits may be actively forming in these areas over interannual timescales. Dark transverse dune deposits adjacent to the north residual cap have relatively low apparent thermal inertias, as do arcuate scarp regions within the polar layered deposits that appear to be major sources of polar dune material. The apparent thermal inertias of these north polar dune deposits are significantly lower than those of intracrater dune deposits at lower latitudes. The north polar dunes are interpreted to be composed of dark unconsolidated material that is being eroded from the layered deposits and transported away from the pole by saltation. The region poleward of 60°N contains no large low thermal inertia regions, which is interpreted as evidence that atmospheric dust is not accumulating in the north polar region under present climatic conditions.

1. Introduction

The temperature of the surface of Mars is one of the most important properties of the planet. Surface temperature is a key parameter when considering the thermal state of the atmosphere and subsurface, and plays a major role in determining the distribution of volatiles. From 1976 to 1980, the Viking infrared thermal mapper (IRTM) instruments [*Kieffer et al.*, 1977; *Chase et al.*, 1978] aboard the two Viking orbiters obtained an extensive set of thermal emission and solar reflectance observations of Mars. In large part, these observations define the thermal state of the planet and its diurnal and seasonal variation. To date, the primary, global-scale analyses of these observations have concentrated on the midlatitude regions from 60°S to 60°N [*Kieffer et al.*, 1977; *Palluconi and Kieffer,* 1981; *Pleskot and Miner,* 1982; *Christensen*, 1988]. There have also been in-depth analyses of the thermal behavior at the residual polar cap regions near the north and south poles [*Kieffer et al.*, 1976a; *Kieffer*, 1979; *Paige and Ingersoll*, 1985], but in general, the IRTM observations of the regions poleward of 60° latitude in both hemispheres have not been systematically investigated. This study presents the first maps of the thermal properties of the Martian surface from 60°N to the north pole. These results, plus those presented in a companion paper [*Paige and Keegan*, this issue] (hereafter referred to as Paper 2), complete the initial thermal mapping of the entire planet.

In the next major section we describe the procedures we have used to map the apparent thermal and reflectance properties of the north polar region of Mars, and describe the results. In the section that follows, we explore the sensitivity of these results to the potential effects of the Martian atmosphere, which were not considered when creating the maps. In the final section, we interpret all of our results in terms of surface physical properties and geological and atmospheric processes.

2. Mapping Apparent Thermal Inertia and Albedo

Fitting observed temperature variations with the results of thermal model calculations has proven to be an extremely useful

Paper number 93JE03428.
0148-0227/94/93JE-03428$05.00

approach in past studies. This procedure enables first-order comparisons between temperature observations obtained at different latitudes, seasons, and local times. It also provides information concerning the thermophysical properties of surface and subsurface materials. This section describes the procedures we employed to fit a set of IRTM observations of the north polar region with the results of a basic Mars thermal model and presents the resulting maps.

Basic Thermal Model

The basic thermal model we employ to fit the IRTM observations is similar in concept to the original diurnal and seasonal Mars thermal model developed by *Leighton and Murray* [1966], and to models used in later studies [*Kieffer et al.*, 1977; *Clifford and Bartels*, 1986; *Paige*, 1992; *Wood and Paige*, 1992]. We have intentionally made it as simple as possible.

During each model time step, surface soil temperatures are determined assuming an instantaneous balance between absorbed solar energy, emitted infrared radiation, and heat conduction from subsurface layers. If surface temperatures fall to the CO_2 frost-point temperature, then a layer of CO_2 frost is assumed to form at the surface, and surface soil temperatures are fixed at the frost-point until the overlying CO_2 frost is completely sublimated. The model assumes that subsurface soil properties are constant with depth, and that all surfaces have unit emissivities, and are opaque to solar and infrared radiation. The atmosphere is assumed to be transparent to radiation at all wavelengths. Conductive heat transfer between surface and atmosphere is ignored, and the heat flow from the Martian interior is assumed to be zero. The CO_2 frost-point temperature is fixed at 148 K, and the latent heat of CO_2 is taken to be 590,000 J kg^{-1}.

In this model, surface temperatures are determined by only a small number of variable parameters, which include the insolation history, the surface CO_2 frost albedo A_f, the surface soil or water ice albedo A_s, and the soil thermal inertia I. The thermal inertia is a composite quantity defined as $I = \sqrt{k\rho c}$, where k, ρ, and c are the thermal conductivity, density, and heat capacity of the soil, respectively.

Previous efforts to map the thermal properties of the midlatitude regions of Mars have used identical assumptions, except for the inclusion of a constant surface heating term to account for the downgoing infrared flux at the surface due to thermal emission from the Martian atmosphere. This heating rate has been taken to be 2% of the local noontime insolation, or 2% of the emitted infrared flux from the surface at the frost-point during the polar night [*Kieffer et al.*, 1977; *Palluconi and Kieffer*, 1981]. The inclusion of this term tends to increase calculated predawn temperatures and prevent excessive nighttime CO_2 frost condensation in midlatitude regions. We chose not to include this term in our basic thermal model for three reasons. (1) Our mapping studies were conducted in locations where excessive predawn condensation was not a serious problem. (2) The results of more detailed atmospheric one-dimensional atmospheric radiative-convective models show that this term may not be a realistic approximation of actual downgoing infrared fluxes at the surface [*Haberle and Jakosky*, 1991]. (3) Fitting the observations using the simplest possible model, that ignores the atmosphere

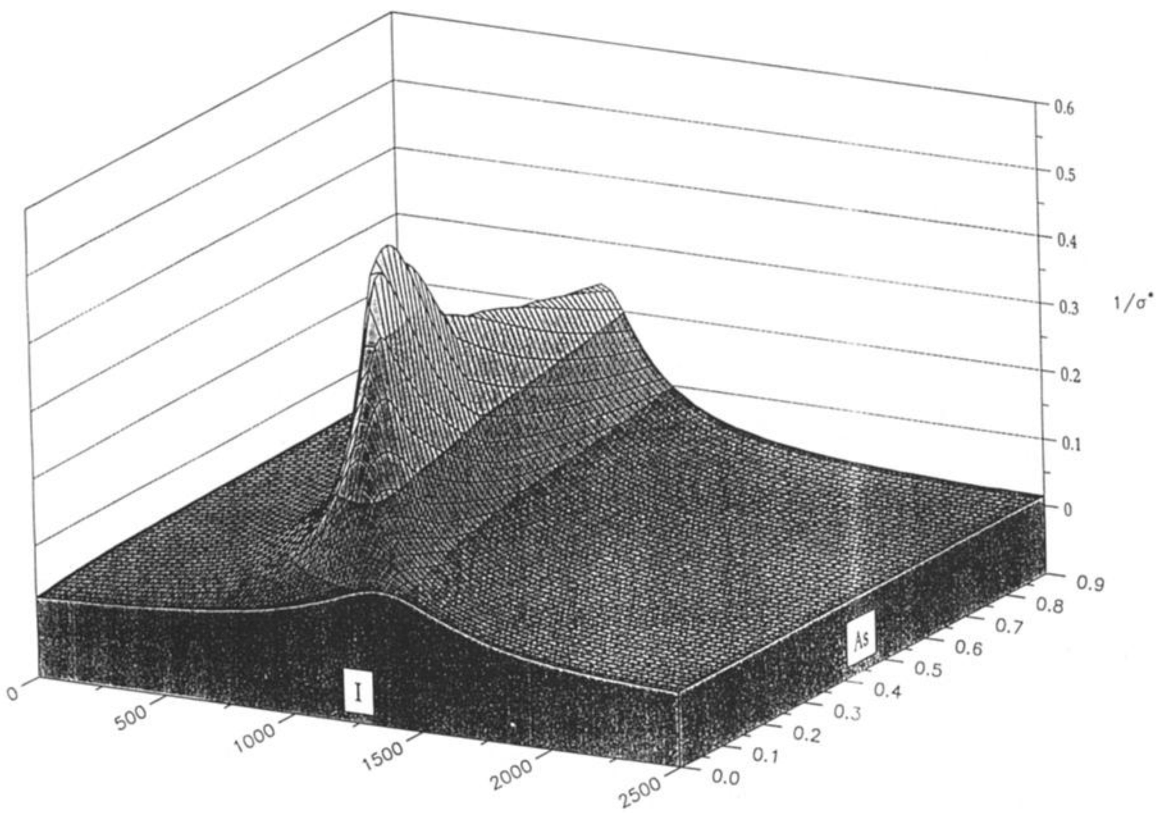

Figure 1. The reciprocal of the standard deviation of the differences between observed and model-calculated temperatures, $1/\sigma*$ as a function of thermal inertia I and surface albedo A_s. This example shows $1/\sigma*$ for IRTM observations of a single, bright, high thermal inertia region centered at 76.56°N, 189.64°W.

completely, makes it easier to describe and understand the net effects of the atmosphere on the surface heat balance, which we address in a later section.

Selection and Processing of IRTM Observations

The IRTM observations used in this study were obtained during a 50-day period of excellent spatial and diurnal coverage that occurred from June 10, 1978, to September 30, 1978 (L_s 98.39 to 121.25, Julian date 2443670 to 2443720). This corresponded to the early summer season in the northern hemisphere when regions northward of approximately 65°N to 68°N were continuously illuminated at the start and end of the period. The north polar residual water ice cap was completely exposed, and polar surface temperatures were at their seasonal maximum [*Paige and Ingersoll,* 1985]. Viking orbiter observations show that the polar atmosphere was relatively clear during this period. Thin hazes, composed of water ice and/or dust were observed, but thick haze clouds were generally absent [*Kahn,* 1984].

The IRTM data from both orbiters were constrained to exclude observations obtained at slant ranges of less than 3500 km and greater than 22,000 km, and emission angles of greater than 78.464°. Approximately 82% of these observations were obtained at slant ranges of less than 14,000 km, and 55% were obtained at slant ranges of less than 8000 km. If the IRTM field of view is taken to be a circle with a diameter of 5.2 mrad [*Chase et al.*, 1978], then the minor axes of the unsmeared fields ranged from 18 to 114 km when projected on the planet. The remaining observations were then grouped into 12,267 mapping regions with boundaries defined by squares with sides of 0.5° of latitude on a simple polar conic projection, where r=(90°- latitude) and θ=(270° - longitude). The choice of region sizes was dictated by trade-offs between coverage, instrument field of view, and the desire to make maps with the best possible spatial resolution. The areas of the mapping regions used in this study are one sixteenth those used by *Palluconi and Kieffer* [1981] from 60°S to 60°N. The total number of observations used was 268,873.

We chose to use the IRTM 20-µm channel brightness temperatures (T_{20}) for thermal mapping and model fitting because of their radiometric precision at cold temperatures, and their relative insensitivity to absorption, scattering, and emission by atmospheric aerosols. The effects of aerosols on T_{20} and thermal inertia are discussed in a later section.

Determining Best Fit Apparent Thermal Inertias and Albedos

The basic thermal model was used to create a five-dimensional table of model-calculated surface temperatures in the north polar region as a function of latitude, season, local time, soil albedo, and thermal inertia. CO_2 frost albedos were fixed at 0.55, which provided a good fit to the observed retreat and disappearance of the north seasonal polar cap during spring [*Christensen and Zurek,* 1984; *Paige and Ingersoll,* 1985]. To create the table, we used a seasonal resolution of 25 sols, a local time resolution of one Mars hour, a latitude resolution of 5° (except poleward of 80°, where it was increased to 2°), a soil albedo resolution of 0.1, and a thermal inertia resolution of 41.86 J m^{-2} s$^{-1/2}$ K^{-1} x 2^n, where n assumed all integer values from 0 to 6. For each region that had more than five T_{20} observations, model-calculated temperatures at the exact latitudes, seasons, and local times of the observations were determined from the lookup table by five-dimensional linear interpolation for a large number of combinations of I and A_s. The combination of I and A_s that provided the best least squares fit to the T_{20} observations within each region were designated I^* and A^*, the best fit apparent thermal inertia and best fit apparent albedo.

Figure 1 shows $1/\sigma*$, the reciprocal of the standard deviation of the differences between observed and calculated temperatures as a function of I and A_s for observations of a single, bright, high thermal inertia region centered at 76.56°N and 189.64°W, which contained 37 T_{20} observations. For the coverage obtained, the sensitivity of the fit to albedo and thermal inertia is quite evident. The excellent spatial and diurnal coverage obtained by the IRTM instruments during this season permitted similar fits to be obtained for most of the regions studied. For all except the highest latitude regions, the amplitudes of diurnal temperature variations greatly exceed seasonal changes in average temperatures during the mapping period. Diurnal temperature variations in excess of 4 K were observed at all latitudes southward of 86°N.

To increase the speed at which I^* and A^* were determined, standard deviations for 256 coarsely spaced combinations of I and A_s were calculated as shown in Figure 2. The best fitting combination was then used as the center point of another 256 less coarsely spaced combinations of I and A_s. This procedure was repeated two additional times to find the best fit. The uncertainties in our derived values for I^* and A^* are difficult to estimate, because they depend to a large extent on the character and coverage of the observations used. Our tests show that at latitudes equatorward of 86°N, the fitting procedure itself introduces uncertainties in I^* and A^* that are less than 5%.

Apparent Thermal Inertia and Albedo Maps

Plates 1 and 2 show maps of the best fit apparent thermal inertia I^* and best fit apparent albedo A^* for the IRTM north polar observations used in this study. The maps of both quantities show considerable structure. The most notable features include (1) the bright north residual water ice cap centered at the pole, which has a very high apparent thermal inertia, (2) the dark north circumpolar dune deposits surrounding the residual cap, which have low to intermediate apparent thermal inertias, (3) the detached bright north polar ice deposits (72° to 80°N, 110°to 270°W), which have very high apparent thermal inertias, (4) the dark northern extension of the Acidalia region (60° to 75°N, 20° to 60°W), which has high apparent thermal inertia at 60°N, but intermediate apparent thermal inertia at 75°N, (5) the bright northern Tharsis region (60°N, 90° to 180°W), which has low apparent thermal inertia.

The number of T_{20} observations per mapping region and the standard deviations of the best fits are shown in Figures 3 and 4. For most regions, the standard deviations were less than 2.5 K. The major exceptions were regions near the boundaries of high thermal inertia ice deposits, which were difficult to fit either because they contained contrasting thermal structure, or because of unknown (but presumably small) errors in pointing knowledge.

Comparisons With Measured Albedos

In addition to thermal emission measurements, the Viking IRTM instruments simultaneously acquired an extensive set of solar reflectance observations of Mars using a broad-band solar channel which spanned the wavelength region from 0.3 to 3.0 μm [*Chase et al.*, 1978]. These data have been used in a variety of previous studies [*Kieffer et al.*, 1977; *Christensen* 1988; *Kieffer*, 1979; *Paige and Ingersoll,* 1985; *Clancy and Lee,* 1991],

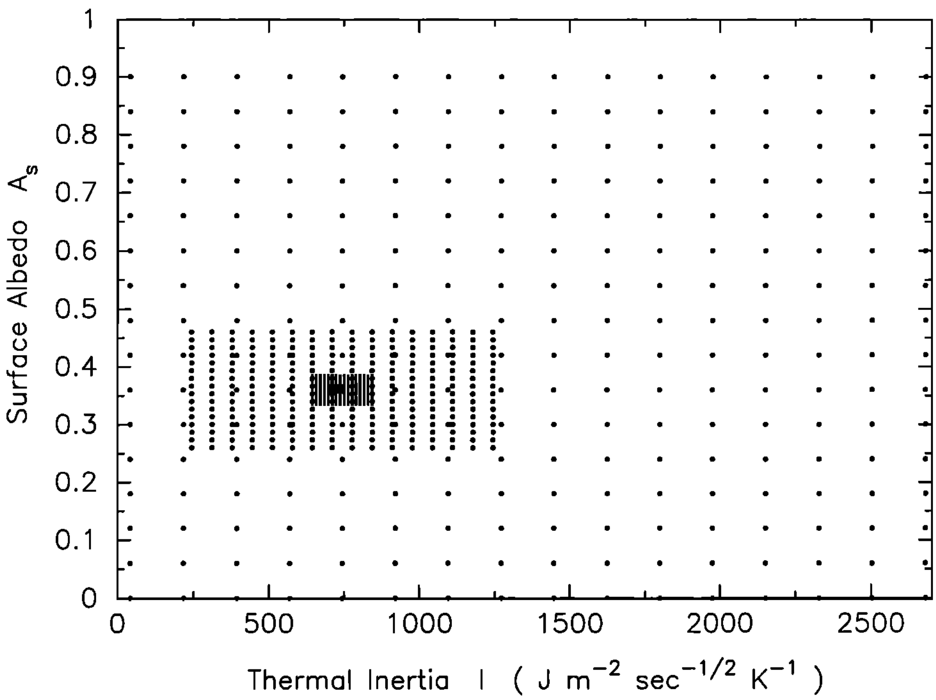

Figure 2. The points represent four successive sets of 256 combinations of thermal inertia and albedo used to determine best fit thermal apparent thermal inertia I^* and best fit apparent albedo A^* for the region used in Figure 1. For this region, I^*=733 J m^{-2} s$^{-1/2}$ K^{-1}, A^*=0.360, and σ^*=1.89 K.

which have included the construction of a map of the "phase-corrected" albedo of Mars from 60°S to 60°N (*Pleskot and Miner,* 1982). In this study, we have used the IRTM solar channel observations to map the Lambert albedo of the north polar region during the mapping period. The map was constructed by excluding all observations that were not used to determine best fit apparent thermal inertias and albedos, and by further excluding observations obtained with local solar zenith angle i of greater than 85°. The measured radiance values in the IRTM solar channels R_{IRTM} were converted to Lambert albedos, A_L by the relation $A_L = F_0 R_{IRTM} / (S_0 \cos i)$ where S_0 is the seasonally varying normal incident solar flux, and F_0 is a constant factor to account for spectral response and absolute calibration [*Kieffer*, 1979]. The Lambert albedo is the ratio of the measured radiance to that expected for a flat, perfectly reflecting, perfectly diffusing surface. Plate 3 shows the average measured Lambert albedos for all regions that had more than one observation. Plate 4 shows the quantity A_L-A_* which is the difference between the averaged measured Lambert albedo based on IRTM solar channel measurements and the best fit apparent albedo based on T_{20} measurements. Figure 5 shows a cross plot of A^* versus A_L for all regions.

In general, the agreement between apparent and measured albedos is good, and the maps of both quantities have a similar appearance. The most notable exceptions occur in regions of lowest apparent inertia northward of 75°N, for which A^* exceeds A_L by over 0.1, and at 60°N, 210°W and 60°N, 340°W, where A_L exceeds A^* by over 0.1.

Comparison With Previous Results

Palluconi and Kieffer [1981] used IRTM observations to map the apparent thermal inertia of Mars from 60°S to 60°N at a spatial resolution of 2° of latitude by 2° of longitude. Figure 6a shows a comparison between best fit apparent thermal inertias for regions between 58°N and 60°N from *Palluconi and Kieffer* [1981] and from this study. Figure 6b shows a comparison between measurement of A_g, the "phase-corrected" albedo from IRTM solar channel measurements from *Pleskot and Miner* [1982] and A^*, the best fit apparent albedo from this study. The agreement for both quantities is good. The lower apparent thermal inertias between 70° and 170°W indicated in this study could potentially be due to a number of factors, including the use of more accurate model fitting procedures, neglecting downgoing infrared radiation at the surface, or temporal variations in apparent thermal inertia due to variations in atmospheric dust loading as discussed below.

Figure 7 shows cross plots of A^* versus I^* for the regions mapped. As has been shown in previous studies, there is a clear anticorrelation between albedo and thermal inertia at lower latitudes [*Kieffer et al.*, 1977, *Palluconi and Kieffer,* 1981]. Near the poles, the anticorrelation breaks down due to the presence of bright, high thermal inertia water ice. Figure 8 shows cross plots of A_L versus I^* for the regions mapped. At high latitudes, the appearance of these plots is very similar to those in Figure 7. The most significant differences occur at latitudes between 60°N and 70°N within regions of intermediate to low apparent thermal inertias which have the highest apparent albedos. Previous attempts to fit thermal model results to IRTM observations in these regions over the complete diurnal cycle have also required high apparent albedos [Ditteon, 1982; Paige, 1992] due to the "anomalous afternoon cooling" phenomenon, which is discussed in greater detail below.

Daily Minimum and Maximum Temperatures

Determining best fit values for I^* and A^* for a given region makes it possible to use the basic thermal model to compute

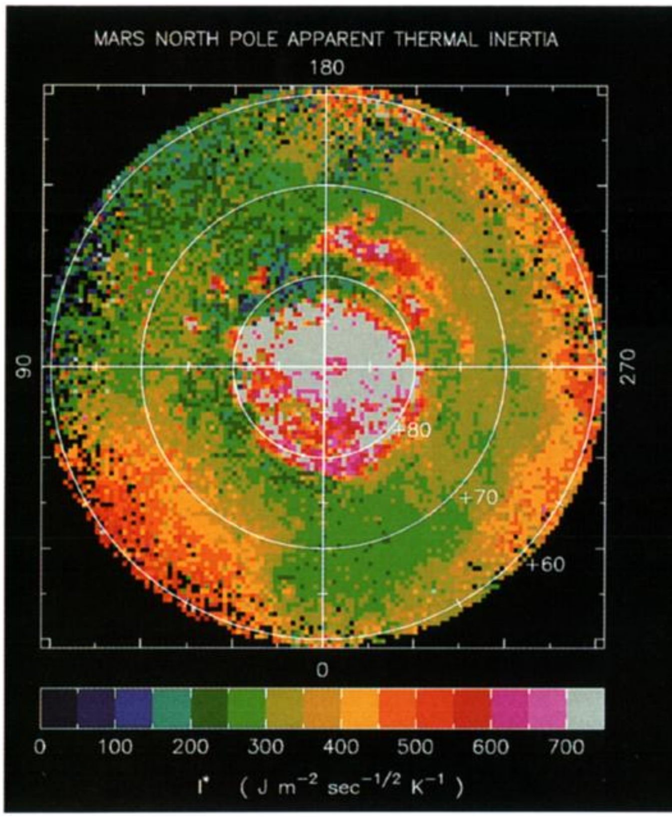

Plate 1. Best fit apparent thermal inertias I^* for the region from 60°N to the north pole. Regions with $I^* > 700$ J m^{-2} s$^{-1/2}$ K^{-1} are colored gray.

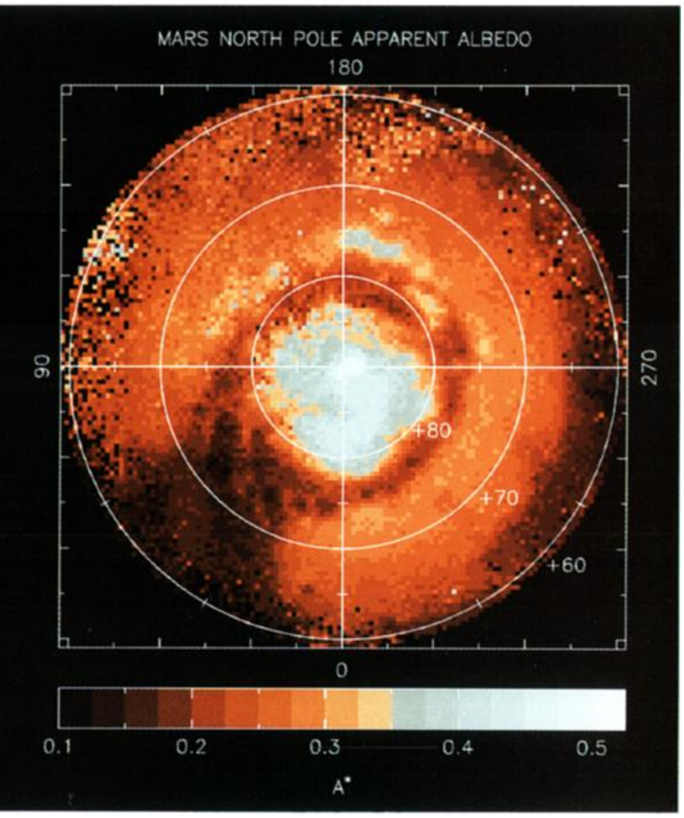

Plate 2. Best fit apparent albedos A^* for the region 60°N to the north pole.

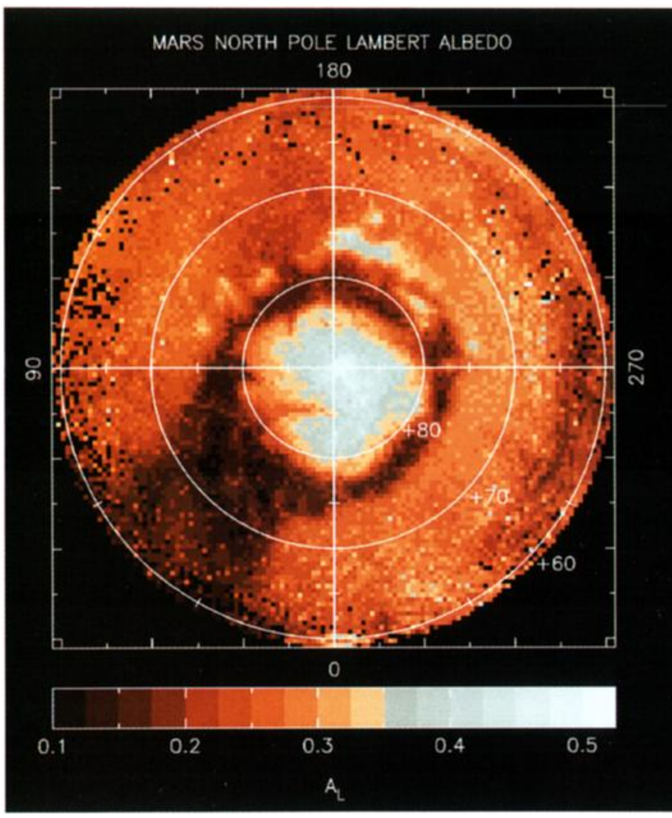

Plate 3. Average Lambert albedo A_L (for the region from 60°N to the north pole.

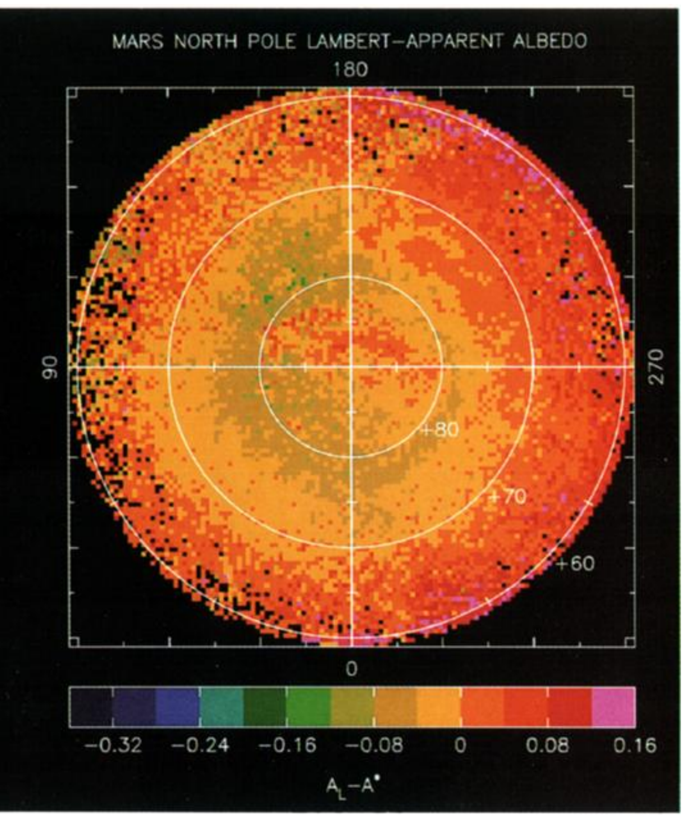

Plate 4. Difference between Lambert albedo and best fit apparent albedo A_L - A^* for the region from 60°N to the north pole.

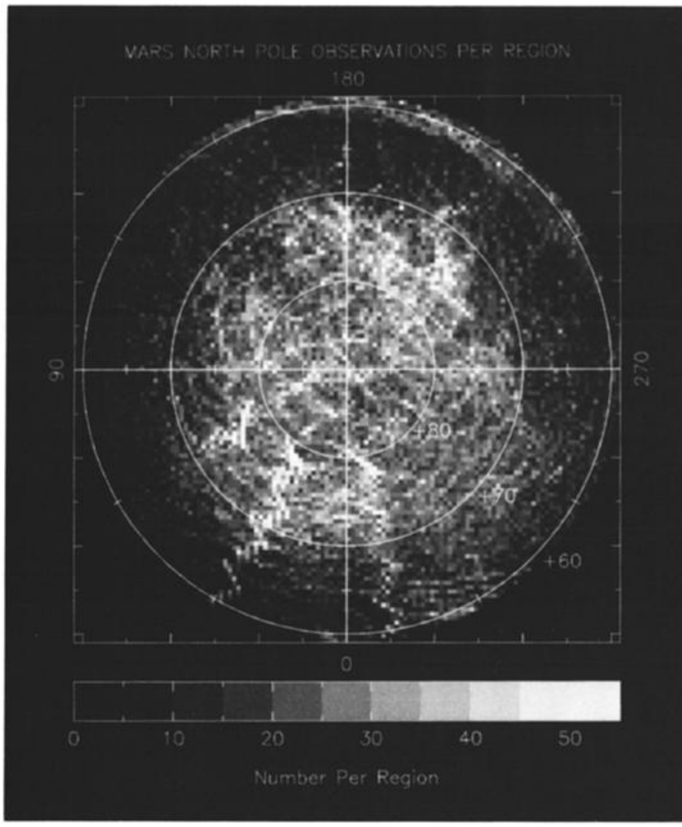

Figure 3. Number of IRTM T_{20} observations for the region 60°N to the north pole.

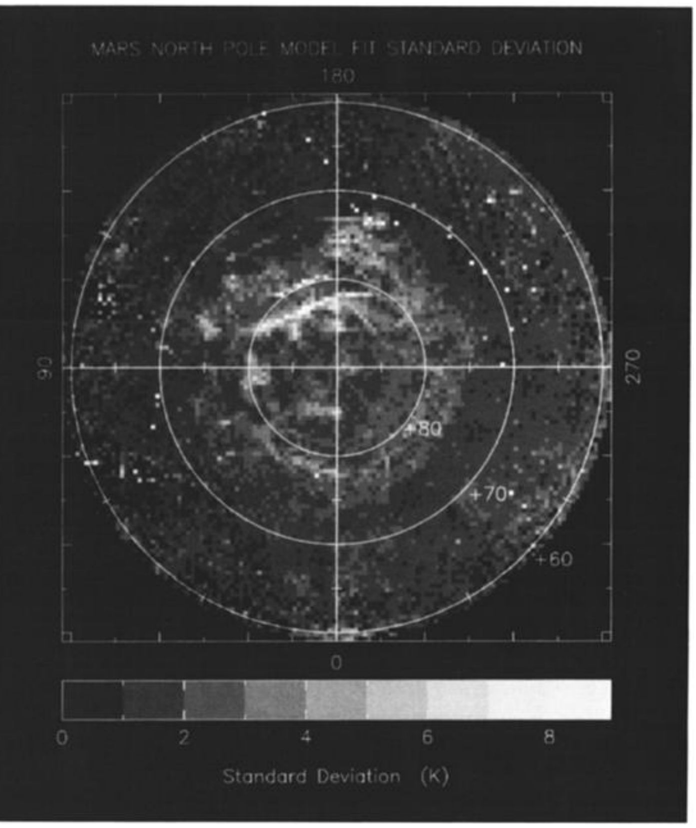

Figure 4. Standard deviations of best fit σ^* for the region from 60°N to the north pole.

temperature variations over a complete diurnal cycle. Plates 5 and 6 show maps of computed daily minimum and maximum surface temperatures (as measured by T_{20}) at Julian date 2443695 (L_s 109.8). The effects of latitude, thermal inertia, and albedo are all evident. Temperatures ranged from 200 to 220 K on the north permanent water ice cap. The highest daily minimum temperatures, in excess of 220 K, were observed in the region surrounding the north permanent cap. The detached bright north polar ice deposits (72° to 80°N, 110° to 270°W) had the same daily minimum temperatures as the surrounding north polar plains. The lowest daily minimum temperatures, close to the 148 K CO_2 frost-point, were observed in the Tharsis low thermal inertia region. Poleward of 70°N, daily maximum temperatures are strongly influenced by albedo. At lower latitudes, daily maximum temperatures are uniformly between 260 and 270 K. Figure 9 shows computed ranges of daily temperature variation as a function of latitude along the 0° and 180° meridians using the same technique. Note that diurnal temperature variations were resolved even within 2° of the north pole.

Comparisons With Surface Features

Figure 10 shows a USGS digital image model projection of the north residual cap area from Viking orbiter images obtained from L_s 110 to L_s 155 during the same Mars year as the IRTM observations used in this study [*U.S. Geological Survey*, 1993]. The features in this image are well correlated with those in the IRTM Lambert albedo map at lower spatial resolution.

Plate 7 shows an enlarged portion of the apparent thermal inertia map superimposed on the surface geologic map of *Tsoar et al.* [1979], which is based on Viking Orbiter imagery of the north polar region. The map shows areas of perennial ice, plains and layered deposits, barchan dunes, transverse dunes, and wind directions inferred from a variety of morphologic indicators. The same region has been mapped separately by *Dial* [1984]. In general, the apparent thermal inertia map is well correlated with surface features in the north polar region. Regions classified as

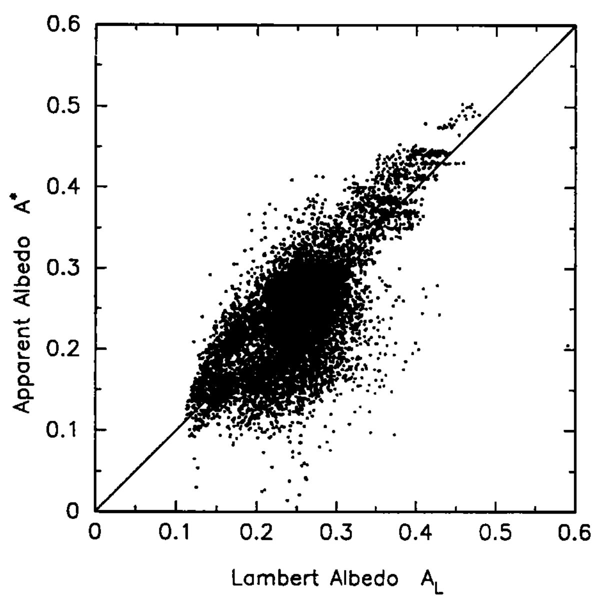

Figure 5. Cross plot of best fit apparent albedo A^* versus measured average Lambert albedo A_L for all regions mapped.

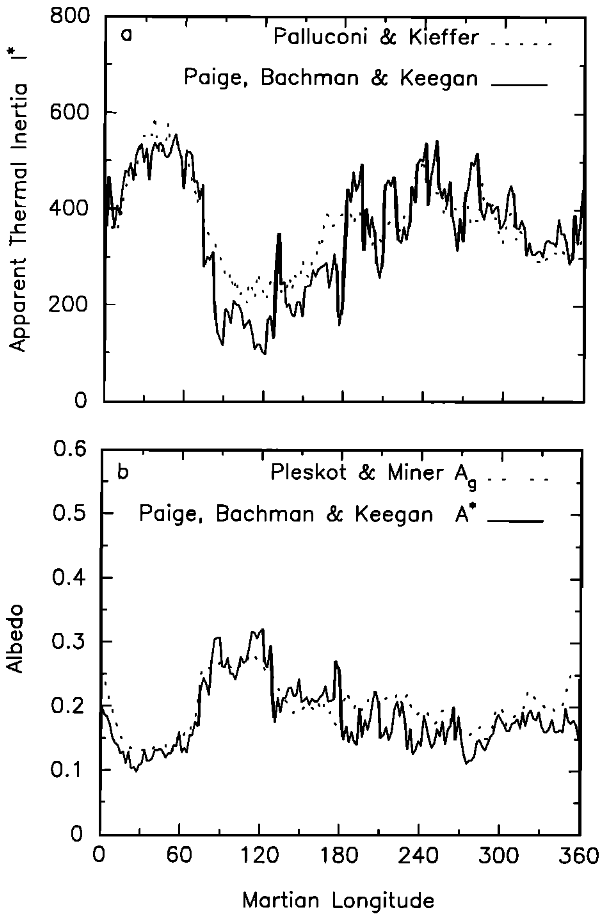

Figure 6. Comparison of the results presented in Plates 1 and 2 and those of previous studies for regions between 58°N and 60°N as a function of longitude. (a) Apparent thermal inertia I^* from Plate 1, and I^* from *Palluconi and Kieffer* [1981]. (b) Best fit apparent albedo A^* from Plate 2, and "phase corrected" albedo A_g from *Pleskot and Miner* [1982].

perennial ice have high apparent inertias. Regions classified as plains and layered deposits have intermediate to high apparent inertias. Regions classified as barchan dunes have intermediate apparent inertias. Regions classified as transverse dunes have low to intermediate inertias.

Residual Diurnal Variability

Although it was possible to obtain values for I^* and A^* that provided a good fit to the IRTM T_{20} observations for most regions, systematic residual differences remained. Figure 11 shows average differences between T_{20} and best fit model-calculated surface temperatures as a function of Mars local time. Figure 11 (top) includes all data for all regions between 60°N and 70°N with I^* between 400 and 550 J m^{-2} s$^{-1/2}$ K^{-1}. Figure 11 (middle) includes all data for all regions between 60°N and 70°N with I^* between 150 and 300 J m^{-2} s$^{-1/2}$ K^{-1}. Figure 11 (bottom) includes all data for all regions between 70°N and 80°N with I^* between 150 and 300 J m^{-2} s$^{-1/2}$ K^{-1}. In each case, the pattern of residual diurnal variability is similar, with T_{20} being 1 to 2 K lower than the best fit model predictions in the late afternoon. This "anomalous afternoon cooling" phenomenon has been well documented at lower latitudes [*Kieffer et al.*, 1977; *Ditteon*,

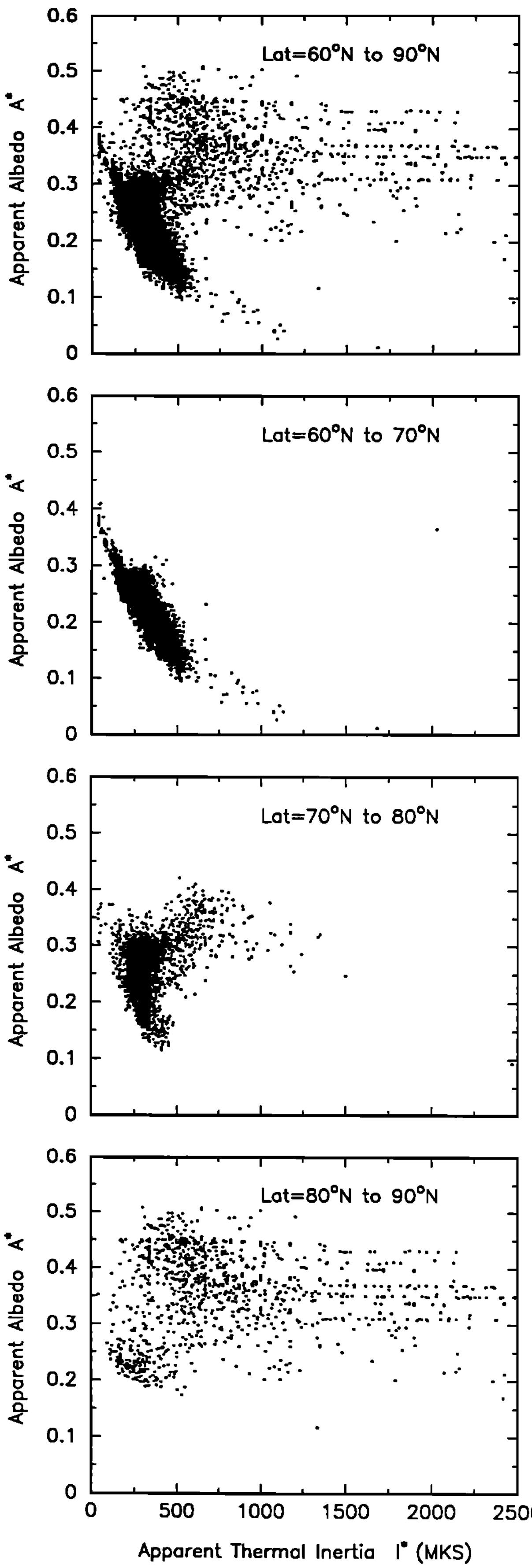

Figure 7. Cross plots of best fit apparent albedo A^* versus best fit apparent thermal inertias I^* for the regions indicated.

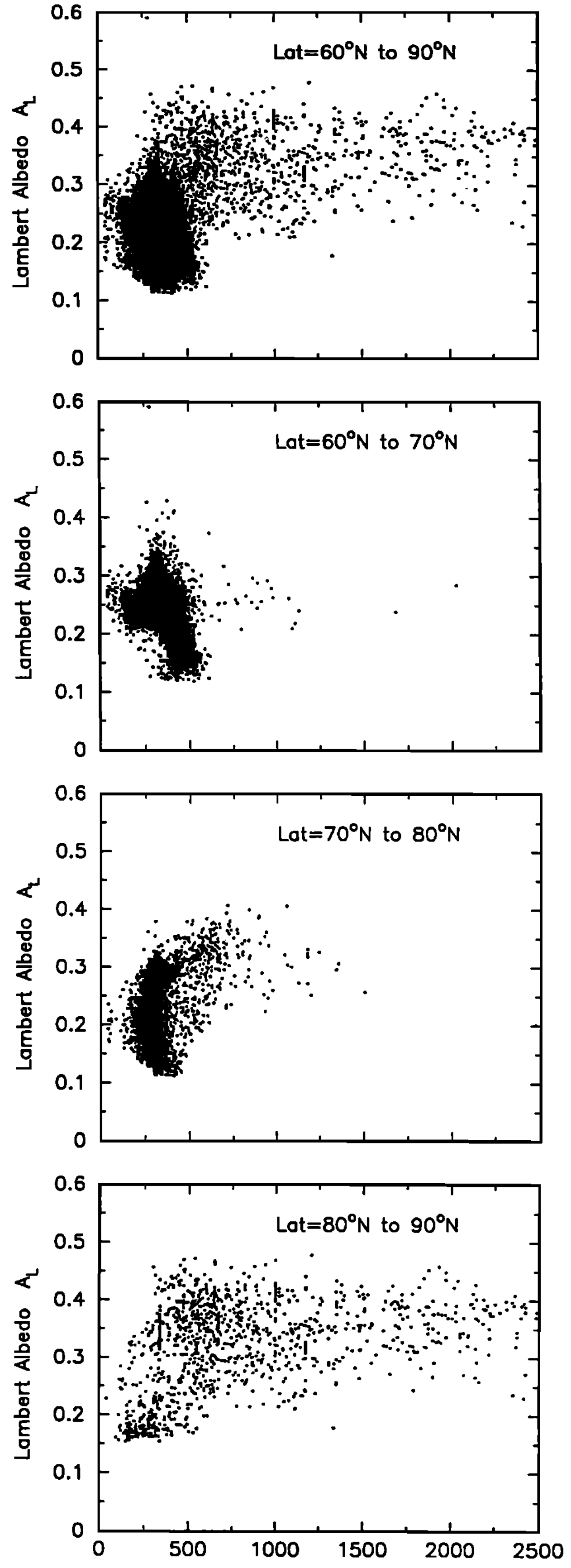

Figure 8. Cross plots of average Lambert albedo A_L versus best fit apparent thermal inertias I^* for the regions indicated.

1982]. In low thermal inertia regions, T_{20} has been observed to be more than 16 K colder than best fit model predictions at 19 hours Mars local time [*Ditteon*, 1982].

Discussion

The maps of the apparent thermal inertia and albedo of the north polar region of Mars presented in this section can be used for many purposes. They show a great deal of spatial structure that is unquestionably due to large variations in the physical properties of polar surface materials. However, the basic thermal model that was used to fit the observations does not account for the effects of the Martian atmosphere, which could be important for determining the temperature of the surface, its rate of thermal emission, and observed IRTM radiances at the top of the atmosphere. Because of these effects, it is not clear whether these new polar observations can be compared directly with published low-latitude observations, or with physical models and parameterizations based exclusively on low-latitude data. In the section that follows, we present a detailed examination of the potential effects of the atmosphere. Then finally, we use this information to interpret our maps of apparent thermal inertia and albedo in terms of surface properties and geologic and atmospheric processes

3. The Effects of the Atmosphere

Understanding the effects of the atmosphere is of great importance for comparing the results obtained here with those of previous studies, and for interpreting the IRTM observations in terms of the true surface thermophysical properties. Previous studies of the effects of the atmosphere can be divided into two categories. The first have dealt with the effects of atmospheric aerosols and/or gases on measured radiances at the top of the atmosphere [*Curran et al.*, 1973; *Toon et al.*, 1977; *Hunt*, 1979; *Santee and Crisp*, 1993]. The second have dealt with the effects of atmospheric radiative and convective heat transfer on surface temperatures [*Pollack et al.*, 1977; *Haberle and Jakosky*, 1991]. The results of both categories of studies indicate that apparent thermal inertias determined from IRTM T_{20} measurements at the top of the atmosphere could differ significantly from the true thermal inertia of the surface. For this study, we have developed a one-dimensional radiative-convective model that includes both effects.

One-Dimensional Radiative-Convective Model

A one-dimensional diurnal and seasonal radiative-convective model was created by integrating the basic thermal model described earlier with a one-dimensional radiative equilibrium model that has been used to investigate atmospheric thermal structure and surface heat balance at the Martian poles [*Paige*, 1985; *Paige and Ingersoll*, 1985]. The model attempts to account for all the major processes that determine the thermal state of the surface and lower atmosphere, including anisotropic-nonconservative scattering by atmospheric aerosols and the absorption by CO_2 gas at solar wavelengths, anisotropic-nonconservative scattering and emission by atmospheric aerosols at infrared wavelengths, emission and absorption by CO_2 gas in the strong 15-μm band, and conductive and convective heat transport between surface and atmosphere. The effects of dynamical motions are not considered, nor are they likely to be of major importance at this season and at this latitude, except for their influence on atmospheric temperatures at higher altitudes.

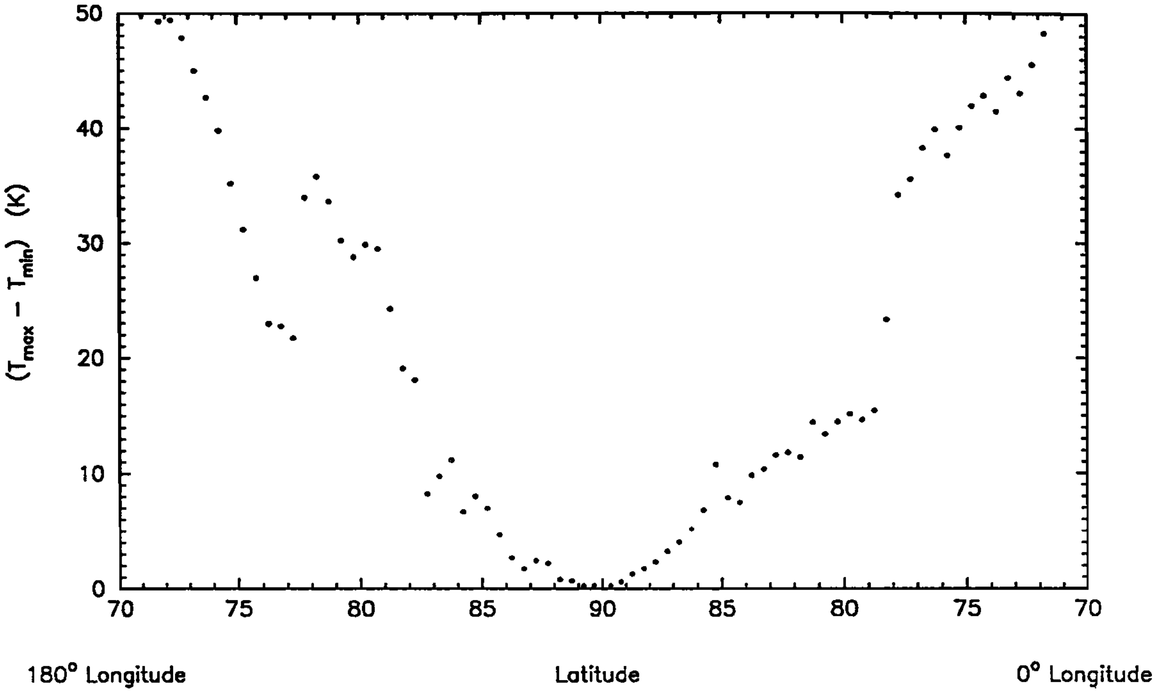

Figure 9. The computed daily range of surface temperature variation (T_{max}-T_{min}) as a function of latitude along the 180° to 0° meridians.

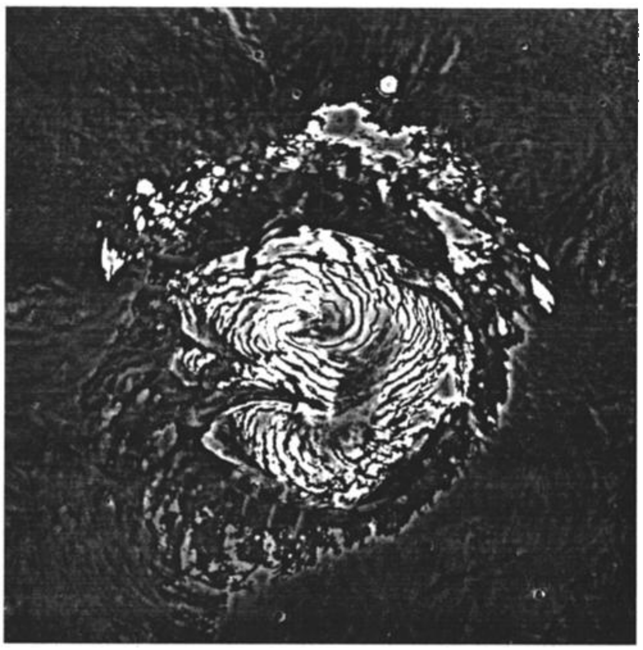

Figure 10. A polar stereographic projection of the USGS 1/16° per pixel digital image model of the north residual cap area from Viking Orbiter images obtained between L_s 110 and L_s 155 during 1978. These images were acquired during the same Mars year as the IRTM observations used in this study.

The model atmosphere consists of a stack of 10 isothermal layers of equal mass overlying a surface with known albedo, thermal inertia, and infrared emissivity. The radiative properties of each layer are fixed, but the temperature of each layer is not. During each model time step, solar heating rates in the 1.316-, 1.455- and 1.600 - μm bands of CO_2 are calculated for each layer according to *Pollack et al.*. [1981]. The solar radiation not absorbed by the near-infrared CO_2 bands is used to calculate surface and atmospheric solar heating rates using a multilayer two-stream δ-Eddington multiple scattering code [*Joseph et al.*, 1976]. Infrared cooling rates for each atmospheric layer in the strong 15- μm band of CO_2 are calculated using the equivalent width parameterization of *Pollack et al.*. [1981]. Infrared cooling rates due to atmospheric aerosols are calculated in seven bands, with three bands from 5.0 to 13.88 μm and four bands from 16.18 to 100 μm. Radiative fluxes are calculated using a modified two-stream δ-Eddington multiple scattering and emission code [*Paige*, 1985] using band-averaged aerosol Mie parameters Plank weighted at 180 K. Aerosol absorption, emission, and scattering are not considered within the core of the CO_2 15-μm band. During each model time step, net radiative heating rates for each layer are used to calculate new atmospheric temperature profiles. If necessary, the new profiles are convectively adjusted in a manner that conserves the total energy of the system. Turbulent heat transfer between the surface and the lowest atmospheric layer is calculated assuming a surface friction velocity of 10 m s^{-1} and the boundary layer parameterizations of *Leovy and Mintz* [1969]. The model components used to calculate the thermal state of the surface and atmosphere are similar to those in the one-dimensional model used by *Haberle and Jakosky* [1991]. As a cross check, a set of test calculations were performed at the latitude of the Viking 1 landing site at L_s 125 with the same model input parameters used to generate Figure 5 of *Haberle and Jakosky* [1991], and identical results were obtained.

After the calculations of the thermal state of the surface and atmosphere were completed, IRTM brightness temperatures at the top of the atmosphere were calculated in a self-consistent manner. IRTM 15-μm channel brightness temperatures, $T_{15,}$ were calculated using the weighting functions presented by *Kieffer et al.*, [1976b], which were originally calculated by Virgil Kunde. IRTM brightness temperatures in the remaining channels (T_7, T_9, T_{11} and T_{20}) were determined using δ-Eddington source functions and the formal solution to the equation of transfer [*Chandrasekhar*, 1960] at a wavelength resolution of 0.1 μm as described by *Paige* [1985].

Model Calculations

The model was run for 18 different combinations of soil and atmospheric properties at six latitudes from 60°N to 85°N. The first set of nine combinations assumed a soil thermal inertia I=83.72 J m^{-2} $s^{-1/2}$ K^{-1} and a soil albedo A_s=0.25. The second set of nine combinations assumed a soil thermal inertia I=272 J m^{-2} $s^{-1/2}$ K^{-1} and a soil albedo A_s=0.25. Table 1 shows nine sets of model atmosphere properties used in the first and second sets of calculations. For model atmosphere 0, the atmosphere was assumed to be nonexistent. The results for model atmosphere 0 are identical to those of the basic thermal model described earlier. For model atmosphere 1, the atmosphere was assumed to contain CO_2 gas, but no aerosols. For model atmosphere 2, the atmosphere was assumed to contain dust with solar spectrum averaged optical properties like those inferred at the Viking 1 landing site during the 1977B global dust storm [*Pollack et al.*, 1979]. At infrared wavelengths, the dust was assumed to have montmorillonite 219B refractive indices from 5 to 15 μm [*Toon et al.*, 1977], and Basalt refractive indices from 15 to 50 μm [*Pollack et al.*, 1973], which proved a good fit to Mariner 9 infrared interferometer spectrometer (IRIS) observations during the 1971A global dust storm [*Toon et al.*, 1977], and to observations obtained by IRTM [*Hunt*, 1979]. Dust infrared optical properties were calculated using Mie theory [*Hansen and Travis*, 1974] assuming a modified gamma size distribution [*Deirmendjian*, 1969] with the size parameters r_m=0.4, α=2, and γ=0.5. These infrared dust optical properties have been used commonly in previous calculations, and in this paper will be referred to as "Mariner 9-inferred" dust. For model atmospheres 2 and 3, the dust was assumed to be distributed uniformly with pressure. Model atmosphere 2 assumes a solar spectrum averaged normal optical depth τ_{so} of 0.2, model atmosphere 3 assumes an optical depth τ_{so} of 0.6. Model atmosphere 4 uses the same dust optical properties, but assumes that the dust is uniformly distributed between the surface and the 3.6-mbar pressure level, which leaves the atmosphere free of dust at altitudes greater than approximately 15 km. Model atmosphere 5 assumes uniform distribution with pressure, but uses a dust size distribution that is more sharply peaked at the smaller radii. This decreases the ratio between the infrared and solar opacity of the dust by a factor of 2. Model atmosphere 6 assumes Mariner 9-inferred infrared dust optical properties, but uses solar spectrum averaged dust optical properties derived by *Clancy and Lee* [1991] from IRTM emission phase function observations. Model atmosphere 7 assumes infrared optical properties and size distribution parameters derived from Mariner 9 IRIS observations of water ice clouds in the Tharsis region [*Curran et al.*, 1973] using water ice refractive indices from *Schaaf and Williams* [1973]. Solar spectrum averaged water ice optical properties were determined for the same size distribution using Mie theory and the refractive index data from *Wiscomb and Warren* [1980]. Model atmospheres 7 and 8 assume the water ice particles are distributed uniformly with pressure. Model atmosphere 7 assumes a solar spectrum average optical depth τ_{so} of 0.2, and model atmosphere 8 assumes a solar spectrum average optical depth τ_{so} of 0.6.

For all cases, the model was run for three Mars years without a radiatively active atmosphere as with the basic thermal model to equilibrate subsurface temperatures until Julian date 2443600 (L_s 68.0), when the north seasonal CO_2 cap was in its final retreat phase. At this point, the atmosphere was "turned on" for 95 days until midway through the mapping period, at Julian date 2443695 (L_s 109.86), and the results for a complete diurnal cycle at all latitudes were recorded. This procedure prevents the different model atmospheres from affecting the date of the complete disappearance of seasonal CO_2 frost, which can influence seasonal temperature variations at high latitudes. Potential seasonal effects were further minimized by considering soils with relatively low thermal inertias.

Results

Figures 12 and 13 show a number of one-dimensional model-calculated quantities during this season as a function of latitude for the eight model atmospheres and the two surface thermal inertias. The results at 60°N and 80°N are presented in numerical form in Tables 2 and 3. Figures 12a and 13a show daily minimum, maximum, and average IRTM 20- μm channel brightness temperatures at the top of the atmosphere for cos *e*, the

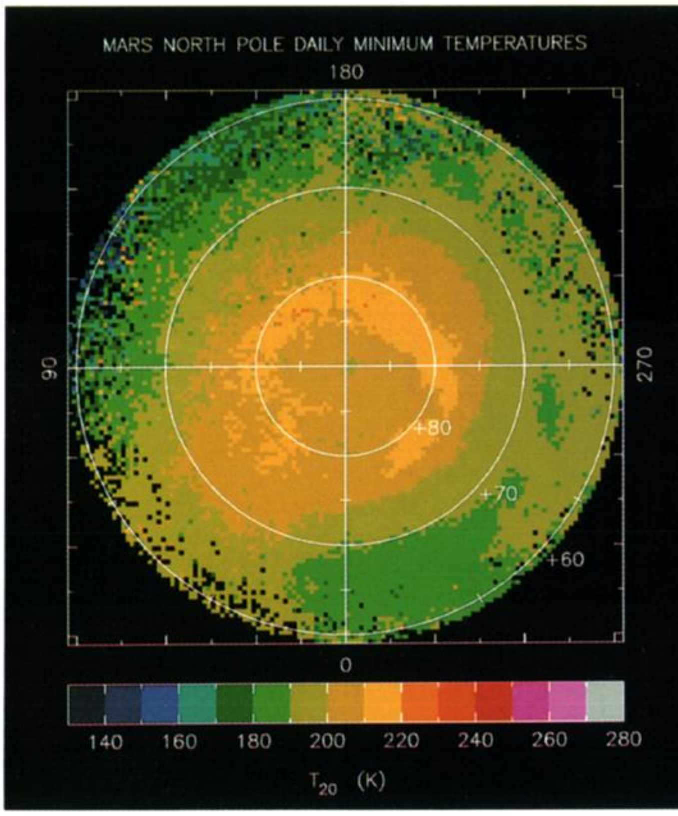

Plate 5. Map of computed daily minimum surface temperatures (as measured by T_{20}) at Julian date 2443695 (L_s 109.8) using best fit values for I^* and A^* inputs to the basic thermal model.

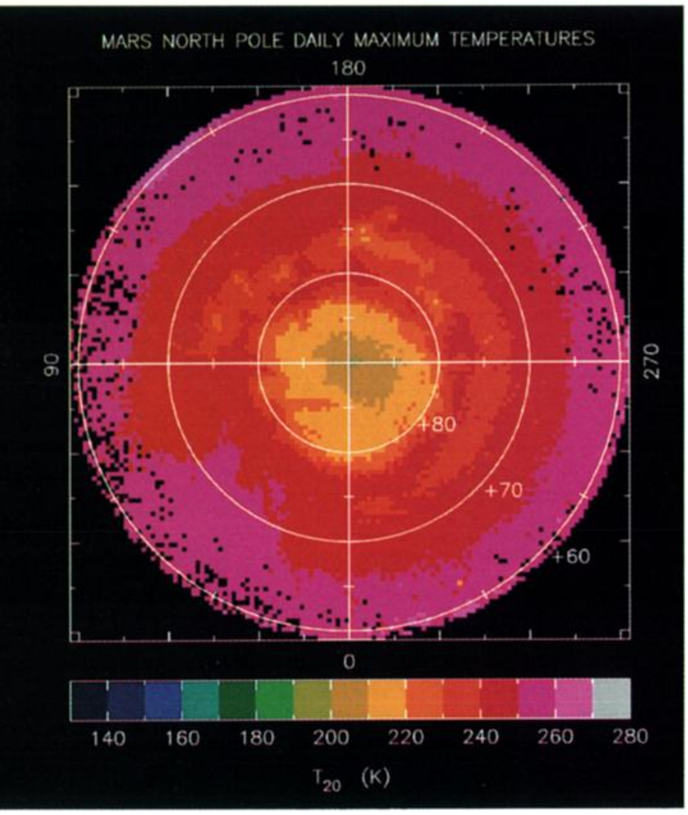

Plate 6. Map of computed daily maximum surface temperatures (as measured by T_{20}) at Julian date 2443695 (L_s 109.8) using best fit values for I^* and A^* inputs to the basic thermal model.

cosine of the emission angle of 0.75. Figures 12b, 12c, 13b, and 13c show basic thermal model best fit thermal inertias I^*, and best fit albedos A^* to the model-calculated T_{20} results. For model atmosphere 0, which assumes no atmosphere at all, the best fit inertias and albedos are equal to the assumed values of the surface thermal inertias and surface albedos at all latitudes. For the other model atmospheres, the best fit inertias are significantly higher than surface thermal inertias. For the same visible opacity, the effects of dust are greater than those of water ice clouds. The effects of dust increase with increasing dust opacity. Best fit albedos are generally lower than actual surface albedos. For model atmospheres 3 and 4, which both assume dust opacities of 0.6, there is a distinct decrease in I^* from 60°N to 85° N during this season. Our results also show that for a given model atmosphere at a given latitude, the difference between I^* and I eventually decreases as I increases. For example, a similar set of model calculations shows that a high inertia surface at 80°N with I=1000 J m^{-2} s$^{-1/2}$ K^{-1} and A_s=0.35 will have an apparent inertia of 1251 J m^{-2} s$^{-1/2}$ K^{-1} when model atmosphere 3 is assumed.

The net effects of the atmosphere on daily minimum, maximum, and average surface temperatures are shown in Figures 12d and 13d. The atmosphere has little net effect on daily maximum surface temperatures at 60°N during this season. For all eight model atmospheres, daily average temperatures at 60°N are of the order of ~10 K higher than the no-atmosphere case for I=83.72, and ~7 K higher for the I=272 case, indicating a modest greenhouse effect. At 60°N, increasing dust visible optical depth from 0 to 0.6 resulted in a ~2 to ~4 K increase in daily average surface temperatures. This is consistent with the results of previous one-dimensional modeling efforts at the Viking 1 landing site, which have predicted dust greenhouse contributions of +4 K [*Pollack et al.*, 1979] and +5 to +7 K [*Haberle and Jakosky,* 1991] for a dust visible opacity of 1.0. It should be noted, however, that for the model atmospheres considered in this study, most of the total greenhouse effect is due to CO_2 gas. One of the most interesting results of these simulations was that dust greenhouse effects become dust antigreenhouse effects at higher latitudes. At 85°N, increasing dust visible optical depths from 0 to 0.6 during this season resulted in a ~3 to ~5 K decrease in daily average surface temperatures. Water ice clouds had similar antigreenhouse effects. This latitudinal variation in the net effects of aerosols is due to the latitudinal variation in insolation during this season. Aerosols decrease the downgoing flux of solar radiation at the surface during the day, and increase the downgoing flux of infrared radiation at the surface at night. High latitude surfaces in perpetual daylight do not experience the enhanced nighttime infrared fluxes and therefore are colder on average. As is demonstrated by the polar radiative equilibrium models of *Davies* [1979] and *Paige and Ingersoll* [1985], the net effects of dust on the surface heat balance also depend on surface albedo.

Figures 12e, 12f, 13e, and 13f demonstrate the importance of accounting for the effects of aerosols on infrared radiances at the top of the atmosphere. Plotted are the quantities I_s^* and A_s^*, which are the best fit apparent thermal inertias and albedos using only the computed surface temperature variations. Comparing the results in Figures 12a and 12b with 12d and 12e with 13a and 13b with 13d and 13e shows that aerosols tend to decrease measured infrared radiances during the day, and increase

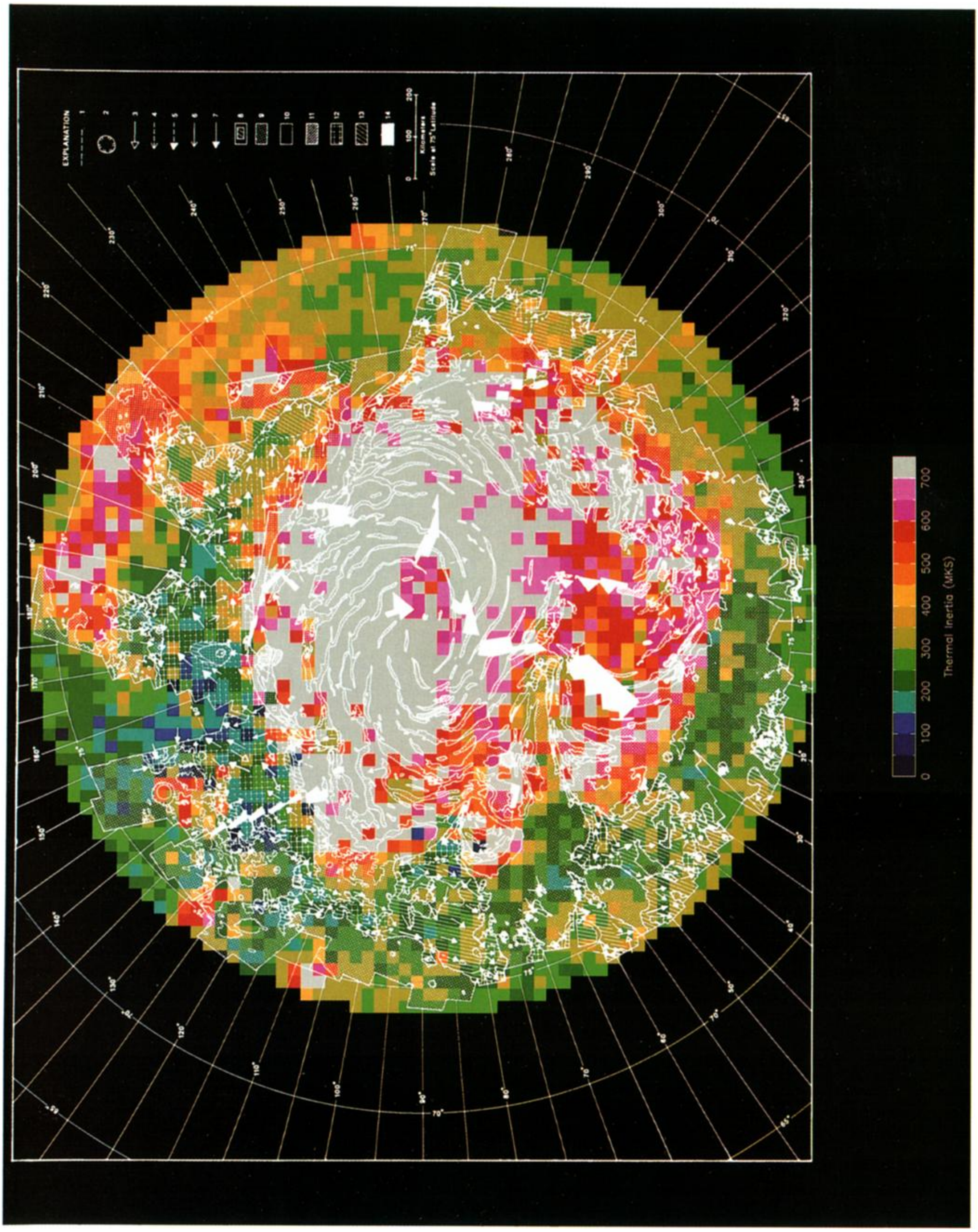
EXPLANATION
Kilometers
Scale at 75° Latitude
Thermal Inertia (MKS)
0
100
200
300
400
500
600
700

measured infrared radiances during the night, resulting in a decrease in the apparent amplitude of diurnal temperature variations and an increase in I^*. In these simulations, the effect was most pronounced for model atmospheres with dust visible optical depths of 0.6. At 60°N, $I_s{}^*$ was 21% to 33% lower than I^* for these cases. Including the effects of aerosols on infrared radiances also affects best fit apparent albedos. Comparing the results in Figures 12c with 12f, and 13c with 13f shows that A^* is distinctly higher than $A_s{}^*$ for most model atmospheric cases. The values of A^* are much closer to the values of the computed solar spectrum averaged planetary albedos at the top of the atmosphere, A_p, which are shown in Figures 12g and 13g. Also, the computed values of A^* and $A_s{}^*$ do not appear to be sensitive to thermal inertia. These relationships may help explain one of the more puzzling results of *Haberle and Jakosky's* [1991] one-dimensional modeling study. These authors were able to use their model to successfully fit a set of IRTM observations at the Viking 1 Lander site, but only for surface albedos between 0.33 and 0.37, which are higher than measured albedos at the top of the atmosphere [*Pleskot and Miner*, 1982]. *Haberle and Jakosky* [1991] expressed concern that this discrepancy could potentially cast doubt on their conclusion that adding dust to the atmosphere results in net surface heating. The results presented in this paper suggest that *Haberle and Jakosky's* need for high surface albedos can be satisfactorily explained by the fact that they ignored the effects of aerosols on measured infrared radiances, and computed only I^* and $A_s{}^*$. In fact, Figures 12 and 13 demonstrate an important general property of planetary greenhouses, which is that they are not easily detectable from remote infrared observations at wavelengths outside of "atmospheric window" regions. For the model atmospheres considered in this study that contain dust, the IRTM 20-μm channel is not located in a completely transparent atmospheric window region, and therefore tends to give calculated daily-averaged brightness temperatures that are T_{20} 1 K lower than calculated daily-averaged surface temperatures during this season.

Figures 14 and 15 show model-computed quantities during this season at 60° N as a function of Mars local time. Figures 14a and 15a show T_{20} - T_{Model}, which are differences between one-dimensional model-calculated IRTM 20-μm channel brightness temperatures at the top of the atmosphere, and best fit basic thermal model surface temperatures. For the no-atmosphere case, the calculated residual diurnal variability is zero. The general pattern of calculated residual diurnal variability displayed for model atmospheres 2 through 8 appears to be largely consistent with the observed residual diurnal variability shown in Figure 11, in that T_{20} - T_{Model} generally tends to be positive from 0 to 3 hours, near zero from 8 to 16 hours, negative from 17 to 21 hours, and then positive from 22 to 24 hours Mars local time. The most scatter in the model-computed T_{20} - T_{Model} values occurs near 5 hours Mars local time. Model atmosphere 4, which assumes a dust opacity of 0.6 confined to the lowest two scale heights, provides the best overall fit. These results tend to support the conclusion of *Haberle and Jakosky* [1991] that the "anomalous afternoon cooling" phenomenon observed at lower latitudes is primarily due to the effects of the Martian atmosphere. Figures 14b and 15b show T_s- T_{Model} which are differences between one-dimensional model-calculated surface temperatures, and best fit basic thermal model temperatures. It should be noted that the similarities of the results in Figures 14a and 14b, and in Figures 15a and 15b are not due to the fact that calculated values of T_{20} and T_s are the same for these cases, but because their deviations from the predictions of the best fitting basic thermal model results are similar.

Atmospheric Temperatures

The eight model atmospheres considered in this study represent only a sampling of a much larger range of possibilities. Choosing the correct model atmosphere to use at a given location and season requires simultaneously acquired information concerning atmospheric properties and structure. For the case of IRTM, independent atmospheric information is available through the 15-μm channel brightness temperatures, which sample a broad range of pressure levels, centered at approximately 0.06 mbar, which corresponds to an altitude of ~26 km [*Kieffer et al.*, 1976b]. *Martin and Kieffer's* [1979] global-scale analysis shows that during nondust storm periods, T_{15} is highest near 17 hours Mars local time, and is lowest near 5 hours Mars local time. The IRTM T_{15} observations of the north polar region during the mapping period showed similar behavior. Figures 16a and 16b show longitudinally averaged T_{15} observations obtained for emission angles of less than 60° between 4 to 6 hours, and 16 to 18 hours, respectively.

Figures 12h and 13h show one-dimensional model-calculated T_{15} values at 5 and 17 hours Mars local time for the eight model atmospheres and two surface thermal inertias. The results show that atmospheric temperatures at this level show no sensitivity to surface thermal inertia, but they show extreme sensitivity to a number of aerosol parameters. As has been demonstrated in previous studies [*Gierash and Goody,* 1972; *Pollack et al.*, 1979], the results for model atmospheres 2 and 3 show that increasing dust opacity increases daily average temperatures at this level, as well as the range of daily variation. The results for model atmosphere 4 show that confining the dust to the lowest two scale heights reduces average temperatures and the range of daily variation. The results for model atmosphere 5 show that decreasing the infrared to solar opacity ratio results in slightly higher atmospheric temperatures due to reduced atmospheric emissivity at infrared wavelengths. The results for model atmosphere 6 show that using the less absorbing dust optical properties proposed by *Clancy and Lee* [1991] results in lower atmospheric temperatures due to reduced atmospheric solar heating rates. Comparing the results for model atmospheres 7 and 8 to those for model atmosphere 1 show that water ice clouds also increase atmospheric temperatures during this season relative to the clear atmospheric case.

Plate 7. An enlarged portion of the map of the apparent thermal inertia I^* of the north polar region of Mars superimposed on the surface geologic map of *Tsoar et al.* [1979]. The map is based on morphology visible in medium-resolution Viking Orbiter images obtained between L_s 132 and 148. Explanation: (1) contact between dune fields; (2) crater; (3) main wind direction determined from springtime images; (4) wind direction determined according to albedo streaks on ice; (5) wind direction based on crater shadow zone; (6) secondary wind direction; (7) main summer wind direction; (8) dunes superposed on ice; (9) plains and layered deposits; (10) perennial ice cap; (11) possible ice dunes; (12) transverse dunes; (13) barchan dunes; (14) no coverage. Regions with I^*>700 J m^{-2} s$^{-1/2}$ K^{-1} are colored gray.

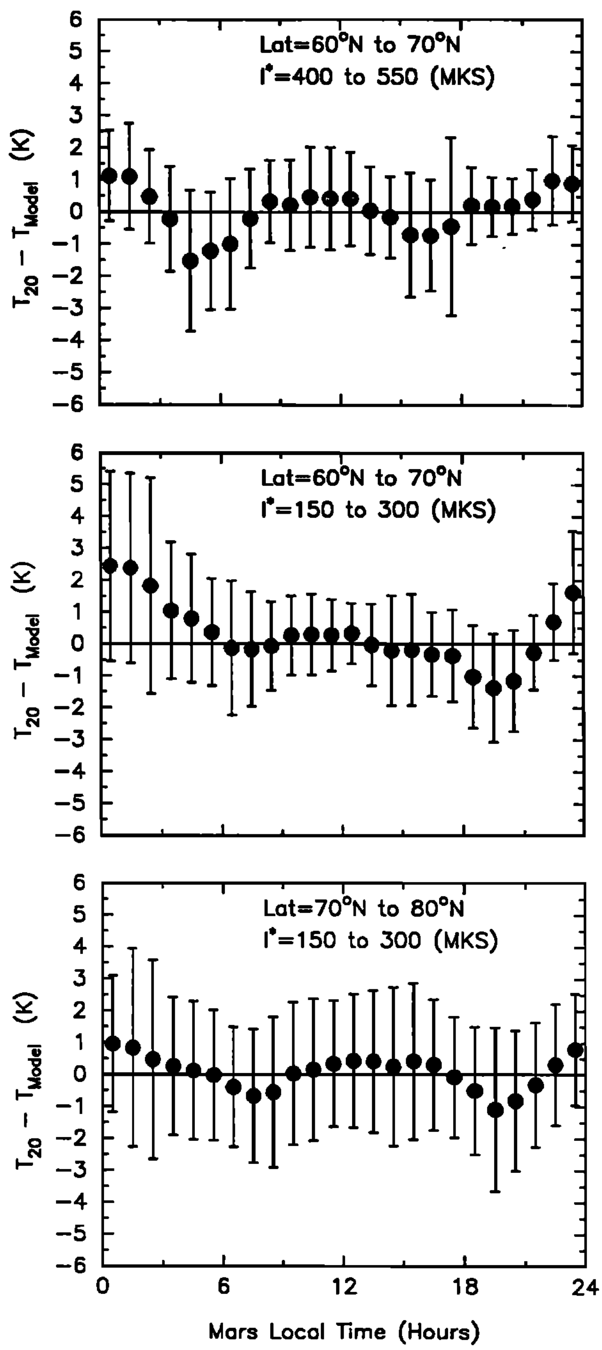

Figure 11. Average differences and standard deviations between observed values of T_{20} and best fit model-calculated surface temperatures as a function of Mars local time for the regions and apparent thermal inertia ranges indicated.

Although the one-dimensional model T_{15} results show trends that can be understood from an intuitive standpoint, none of the eight model atmospheres used in this study gives calculated atmospheric temperatures that are in good agreement with the IRTM T_{15} measurements during this season at all latitudes. In particular, the model atmospheres that can reproduce the large diurnal amplitudes observed in T_{15} at 60°N have atmospheric temperatures that are higher than observed, particularly at the north pole. The exact cause(s) of this discrepancy cannot be identified uniquely. Possible explanations, in roughly decreasing order of likelihood include (1) aerosol optical properties and optical depths varied with latitude and altitude during this season, resulting in lower atmospheric solar heating rates at higher latitudes. (2) Large-scale atmospheric motions played an important role in determining atmospheric temperatures at this level. Such motions were suggested by *Pollack et al.* [1979] as an explanation for why their one-dimensional model also gave higher atmospheric temperatures in this level than were observed during the Viking 1 lander entry. Tidal effects may also influence temperatures at these altitudes [*Leovy and Zurek,* 1979]. (3) The true optical properties and vertical distributions of atmospheric aerosols were unlike those assumed in the eight model atmosphere cases. (4) The approximate techniques used to calculate atmospheric cooling and heating rates in the one-dimensional model may not have been adequate, particularly in the neighborhood of the 15-μm band of CO_2 [*Crisp et al.*, 1986].

Discussion

The one-dimensional modeling results presented here indicate that the effects of the Martian atmosphere on measured diurnal brightness temperature variations are even more significant than those indicated in the study by *Haberle and Jakosky* [1991]. They also demonstrate that aerosol optical properties, vertical distribution, latitude, and season are very important when considering the effects of the atmosphere on surface heat balance. From a practical standpoint, this represents a formidable problem for the analysis of the IRTM north polar observations considered in this study, or for that matter, any other set of infrared observations. While the one-dimensional model results resemble many aspects of the IRTM observations during this season, they are extremely sensitive to the aerosol optical properties and optical depths used in the model atmospheres. The possibility that these properties exhibited significant spatial variability during the mapping period is an additional complicating factor. In the interpretations that follow, the best fit apparent thermal inertias at all latitudes will be treated as upper limits for actual surface thermal inertias, especially for regions with low apparent thermal inertias.

In the future, efforts to map the thermal behavior of the Martian surface would be greatly aided by the acquisition of detailed, simultaneous information concerning the vertical temperature and opacity structure of the lower atmosphere. The acquisition of vertical temperature profiles would also enable the interpretation of multispectral infrared radiance measurements at the top of the atmosphere in terms of aerosol optical properties and optical depths, as has been accomplished using Mariner 9 IRIS observations [e.g., *Toon et al.*, 1977; *Curran et al.*, 1973; *Santee and Crisp*, 1993].

4. Interpretation

The maps of apparent thermal inertia and albedo presented in this study provide new information concerning the properties of the surface and subsurface materials in the north polar region. In this section, we first review some basic relationships between bulk thermal properties and surface thermal behavior, and then we interpret our new thermal inertia and albedo maps in light of previous work and the atmospheric modeling results just presented.

Interpretation of Thermal Inertia

Thermal inertia is a composite quantity that can be affected by a number of factors. For most geologic materials, the volume heat capacity ρc varies by only a factor of 4, which implies that thermal inertia variations are primarily due to variations in thermal conductivity. For particulate surfaces, thermal conductivity can vary widely with grain size, gas pressure, and temperature [*Wechsler and Glaser,* 1965]. Table 4 presents a compilation of estimates for the expected variation in thermal inertia with mean effective particle diameter for unconsolidated silicate materials at typical Martian atmospheric surface pressures [*Edgett and Christensen,* 1991; *Haberle and Jakosky,* 1991]. If interparticle bonding is present, thermal inertias are expected to increase significantly [*Kieffer,* 1976; *Jakosky and Christensen,* 1986]. The measured thermal inertia of a terrestrial sandstone sample [*Carslaw and Jaeger,* 1959] may be representative of the effects of nearly complete interparticle bonding. Also shown is the expected thermal inertia of pure, solid water ice at Martian polar temperatures from *Kieffer* [1990].

A key parameter for the interpretation of thermal inertia determinations from surface temperature variations is β^{-1}, the skin depth for the penetration of periodic temperature waves. $\beta^{-1} = (kP / \pi \rho c)^{1/2}$, where P is the dominant period of surface temperature oscillation, which for diurnal temperature variations is 1 sol, and for seasonal temperature variations is 1 year. If the product ρc is assumed to be 1×10^6 J m^{-3} K^{-1}, then the diurnal skin depth goes as 1.67×10^{-4} I, which is approximately 1.6 cm for a homogeneous low thermal inertia surface with I=100 J m^{-2} s$^{-1/2}$ K^{-1}, or approximately 20 cm for a homogeneous high thermal inertia surface with I=1250 J m^{-2} s$^{-1/2}$ K^{-1}. On Mars, seasonal temperature waves penetrate 25.9 times deeper than diurnal temperature waves.

For surfaces with vertically inhomogeneous bulk thermal properties, the situation is more complicated. Figure 17 shows the results of a series of two-layer thermal model calculations, in which a thin, low thermal inertia surface layer with I=100 J m^{-2} s$^{-1/2}$ K^{-1} was assumed to overlie a semi-infinite, high thermal inertia layer with I=1000 J m^{-2} s$^{-1/2}$ K^{-1}. The latitude is 80°N and the season is midway through the mapping period. The surface albedo is assumed to be 0.4, and the product ρc is assumed to be 1×10^6 J m^{-3}K^{-1} at all depths. Plotted are best fit thermal inertias and albedos from the basic thermal model as a function of the thickness of the low thermal inertia surface layer. The results show that a relatively thin layer of low thermal inertia material can "mask" the presence of high thermal inertia material below. The minimum thickness for nearly complete masking is of the order of one half the diurnal skin depth for the low inertia material [*Ditteon*, 1982]

North Polar Water Ice Deposits

In the north polar region, bright water ice deposits are found on the surface of the north residual polar cap, and in detached regions at latitudes as low as 73°. These deposits all have very high apparent thermal inertias, typically ranging from 600 to 2000 J m^{-2} s$^{-1/2}$ K^{-1}, which are close to the expected thermal inertia of pure water ice at these temperatures (see Table 4). The atmospheric modeling results presented in the last section showed that these very high apparent thermal inertias cannot be due solely to the effects of the atmosphere.

Based on the modeling results presented in Figure 17, it appears safe to conclude that these deposits consist of dense, coarse grained, or compacted snow or ice that extends from the surface, or at least from within a few millimeters of the surface, to depths of at least 10 cm below the surface. This interpretation holds equally for the ice deposits on the residual cap as it does for the detached ice deposits at lower latitudes, which have similar

Table 1. Model Atmosphere Properties

Model Atmosphere	Aerosol Solar Parameters: τ_{so}	Q_{ext}	ϖ_0	g	Aerosol IR Refractive Index Data	Size Distribution Parameters: r_m	α	γ	Aerosol Vertical Distribution, mbar	Comments
0	-	-	-	-	---	-	-	-	-	No atmosphere
1	0.0	-	-	-	---	-	-	-	-	CO_2 gas but no aerosols
2	0.2	2.74	0.79	0.86	Mariner 9-inferred dust	0.4	2	0.5	6.0 - 0.0	Standard dust case τ_{so}=0.2
3	0.6	2.74	0.79	0.86	Mariner 9-inferred dust	0.4	2	0.5	6.0 - 0.0	Standard dust case τ_{so}=0.6
4	0.6	2.74	0.79	0.86	Mariner 9-inferred dust	0.4	2	0.5	6.0 - 3.6	Dust confined to lowest two scale heights
5	0.2	2.74	0.79	0.86	Mariner 9-inferred dust	0.4	2	1.0	6.0 - 0.0	Smaller dust particles
6	0.2	2.74	0.92	0.55	Mariner 9-inferred dust	0.4	2	0.5	6.0 - 0.0	*Clancy and Lee* [1991] dust
7	0.2	2.371	0.9897	0.828	Curran water ice	0.4	2	0.5	6.0 - 0.0	Standard water ice case τ_{so}=0.2
8	0.6	2.371	0.9897	0.828	Curran water ice	0.4	2	0.5	6.0 - 0.0	Standard water ice case τ_{so}=0.6

τ_{so}, Q_{ext}, ϖ_0 and g are the solar spectrum averaged aerosol optical depth extinction efficiency single scattering albedo and asymmetry parameter, r_m is the mode radius and α and γ are shape parameters for modified gamma particle size distributions [*Deirmendjian* 1969]

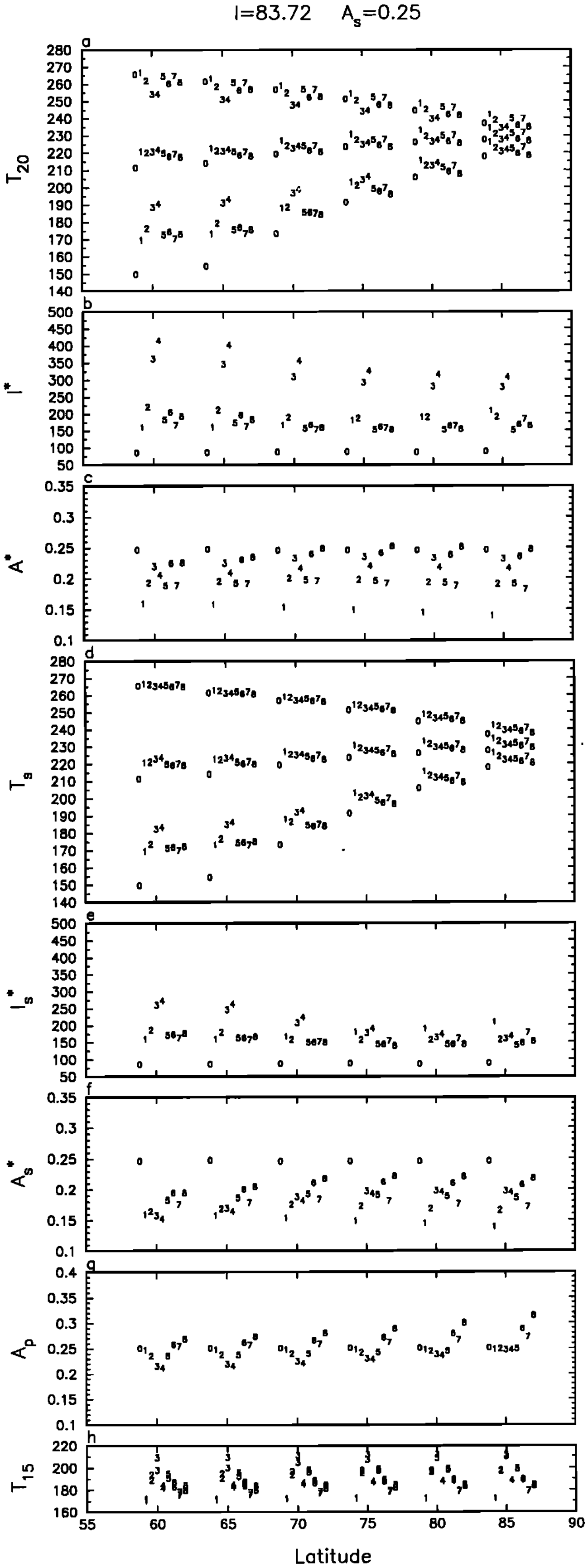

Figure 12. One-dimensional radiative convective model results as a function of latitude at the midpoint of the mapping period at L_s 109.86. Numeric symbols represent the results for the corresponding model atmospheres in Table 1. The symbols are offset horizontally from their true latitudes at 60°, 65°, 70°, 75°, 80°, and 85° for clarity. The surface thermal inertia was assumed to be 83.72 J m^{-2} s$^{-1/2}$ K^{-1} and the surface albedo was assumed to be 0.25 for all cases. (a) Daily minimum, maximum, and average IRTM 20-μm channel brightness temperatures at the top of the atmosphere for cos e = 0.75. (b) Best fit apparent thermal inertia I^* using one-dimensional model-calculated IRTM 20-μm channel brightness temperatures at the top of the atmosphere. Model atmosphere zero is the basic thermal model, which assumes no atmosphere is present. (c) Best fit apparent albedo A^* using one-dimensional model-calculated IRTM 20-μm channel brightness temperatures at the top of the atmosphere, and the basic thermal model. (d) Model-calculated daily minimum, maximum, and average surface temperatures T_S. (e) Best fit apparent thermal inertia I_s^* using one-dimensional model -calculated surface temperatures, and the basic thermal model, which assumes no atmosphere is present. (f) Best fit apparent albedo A_s^* using one-dimensional model-calculated surface temperatures, and the basic thermal model. (g) Planetary albedo A_p at the top of the atmosphere. (h) One-dimensional model-calculated IRTM 15-μm channel brightness temperatures at the top of the atmosphere at cos e = 0.75 at 5 hours, and 17 hours Mars local time.

apparent thermal inertias. It is interesting to note that ice deposits at the north pole, which experience only seasonal temperature variations, have approximately the same apparent inertias as ice deposits at the edge of the cap and in detached regions, which experience significant diurnal temperature variations. This suggests that high thermal inertia material extends to depths of at least 1 meter below the surface of the residual cap. This conclusion is supported by the results of *Paige and Ingersoll* [1985], who used IRTM surface temperature and annual radiation balance measurements to estimate that, to seasonal skin depths, the thermal inertia of the circular region from 86°N to the pole is approximately 1250 ± 400 J m^{-2} s$^{-1/2}$ K^{-1}. This is in excellent agreement with the results of this study, which shows that the average apparent inertia of the same region is 1151 J m^{-2} s$^{-1/2}$K^{-1}.

The fact that the Martian north permanent water ice cap contains coarse-grained or solid water ice is consistent with the model predictions of *Kieffer* [1990]. By scaling field-verified models for thermal metamorphism rates of terrestrial snow, *Kieffer* [1990] predicts steady state surface ice grain radii ranging from 90 μ m to 3 mm for present Martian conditions at 85°*N*. *Kieffer* [1990] also shows that since the average mass loading of dust in the Martian atmosphere is comparable to the average mass loading of water vapor [*Pollack et al.*, 1979], dust/ice mixtures deposited onto the north polar cap in their expected atmospheric proportions would be expected to have considerably lower albedos than observed. *Kieffer* [1990] favors two possible explanations for the relatively high albedo of the Martian north permanent cap. The first is that the uppermost centimeters of the cap consist of a metamorphosed, coarse-grained deposit of nearly pure water ice. The second is that the top surface of the permanent cap consists of an admixture of recently deposited, fine-grained snow particles and small quantities of atmospheric dust. The most straightforward interpretation of the apparent thermal inertia measurements presented in this paper would favor the first explanation. However, the second explanation cannot be completely ruled out. Both laboratory and modeling studies show that surface layers of fine-grained snow that are less than 1

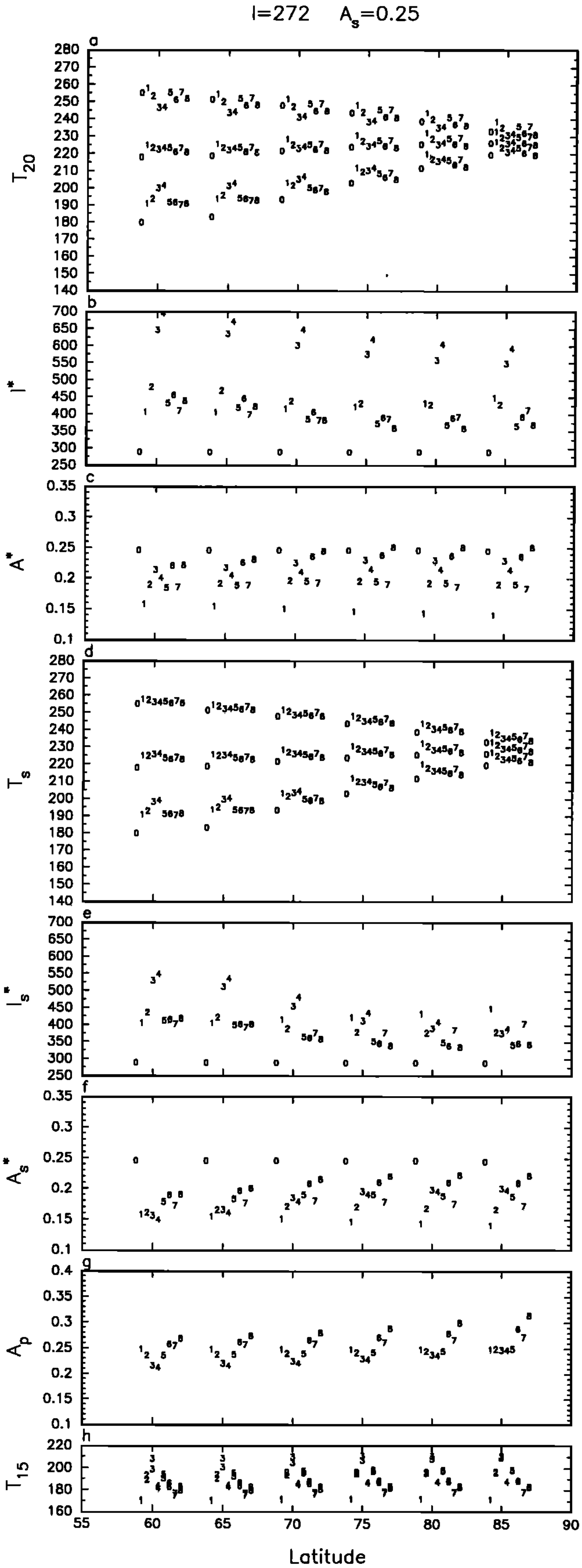

Figure 13. Same as Figure 12, assuming a surface thermal inertia of 272 J m^{-2} s$^{-1/2}$ K^{-1}.

mm thick can effectively mask the presence of darker underlying material [*Wiscomb and Warren,* 1980; *Clark*, 1980]. The results in Figure 17 show that the presence of a thin, fine-grained, low-inertia surface layer cannot be discounted on the basis of the apparent thermal inertia measurements. Whichever explanation is correct, the thermal inertia measurements definitely imply the presence of significant quantities of dense, coarse-grained water ice close to the surface.

Thermal Inertias of North Polar Layered Deposits

From the standpoint of Mars climate studies, the polar layered deposits are of great interest. These deposits, which are found in both the north and south polar regions, consist of layers of presumed depositional origin that can be traced for hundreds of kilometers [*Murray et al.*, 1972; *Cutts*; 1973; *Howard et al.*, 1982]. The finest layers that can be resolved in the best available imagery have thicknesses of approximately 15 m [*Dzurisin and Blasius,* 1975; *Blasius et al.*, 1982], and finer-scale layering is likely to be present. The existence of these layers has been widely attributed to climatically driven variations in the rates of deposition and erosion of airborne sediments in the polar regions due to quasi-periodic variations in Mars orbital and axial elements [*Ward*, 1974; *Ward et al.*, 1974; *Toon et al.*, 1980; *Carr*, 1982]. The deposits themselves contain few visible impact craters [*Cutts et al.*, 1976; *Plaut et al.*, 1988], and the ages, accumulation rates, and erosional histories of these deposits are highly uncertain.

The physical makeup of the layered deposits has proven to be difficult to determine. In the north polar region, layered deposits are intimately associated with the north permanent water ice cap, and boundaries between these two units are often not well defined. In the north, these deposits are exposed in dark arcuate troughs and scarps within the permanent cap, and in flatter regions at the cap's periphery that have intermediate albedos. In the south, layered deposits are exposed within the residual cap and over a wide frost-free region that surrounds the cap during the summer season. Existing observations provide few constraints on the composition of the layered deposits [*Thomas et al.*, 1992]. They are generally believed to be an admixture of unknown proportions of ice, dust, and sand [*Carr*, 1982; *Malin*, 1986; *Thomas and Weitz*, 1989; *Hofstadter and Murray,* 1990].

In the north polar region, the largest areal exposures of layered terrain occur in regions of intermediate albedo at the edge of the residual cap on either side of the mouth of Chasma Boreal near 88°N, 75°W, and at 79°N, 40°W, and further west at 79°N, 105°W. These layered terrain regions can be clearly seen in the USGS photomosaic of the residual cap area (see Figure 10), and are also visible in the IRTM Lambert albedo map (see Plate 3). Despite the lower albedos of these layered terrains, the results presented in Plates 1 and 7 show their apparent thermal inertias are quite high. The equatorward boundaries of these regions are marked by abruptly lower apparent thermal inertias, which coincide exactly with the albedo boundaries shown in Plate 3 and Figure 10. The average apparent thermal inertias of the 38 mapping regions completely within the largest continuous layered terrain region near 79°N, 40°W is approximately 565 J m^{-2} s$^{-1/2}$ K^{-1}. For comparison, the highest apparent thermal inertias determined by *Palluconi and Kieffer* [1981] in their study for regions between -60°N and 60°N were 630 J m^{-2} s$^{-1/2}$ K^{-1}.

The high apparent thermal inertias of the exposed north polar layered deposits imply that, to at least a diurnal skin depth, these deposits are probably not composed solely of unconsolidated dust or sand. The fact that the layered deposits have distinctly higher apparent inertias than the surrounding dark circumpolar dune deposits or adjacent polar plains areas is consistent with this interpretation. If the layered deposits are sedimentary in origin, their high thermal inertias imply the presence of a bonding agent, which could potentially be a weathering byproduct [*Herkenhoff and Murray,* 1990] or water ice itself. The ubiquity of water ice in the north polar region makes ice a prime candidate for the bonding material. The high thermal inertias of these deposits could also indicate that these deposits consist of dust-contaminated ice. Given that the average mass loading of dust in the Martian atmosphere is comparable to the average mass loading of water vapor [*Pollack et al.*, 1979], dust/ice mixtures deposited onto the north polar cap in their observed atmospheric proportions would be expected to have low albedos [*Kieffer*, 1990].

Water Ice Stability in the North Polar Layered Deposits

A number of authors have pointed out that near-surface water ice may not presently be stable to evaporation in dark regions adjacent to the cap [*Kieffer et al.*, 1976a; *Toon et al.*, 1980; *Haberle and Jakosky,* 1990; *Hofstadter and Murray,* 1990]. The new observations presented in this paper enable us to examine the potential stability of ice within these terrains in greater detail than has previously been possible.

The Mars atmospheric water detector (MAWD) observations of the north polar region during the Viking primary mission revealed the presence of abundant water vapor in the north polar region during the summer season [*Farmer et al.*, 1976]. More detailed observations obtained simultaneously with the IRTM observations used in this study during the second Viking year showed significant spatial variability in column water vapor abundances [*Davies*, 1982]. During the mapping period, column water vapor abundances were typically 25 to 50 precipitable microns (pr.-μm) over the bright regions of the north residual cap, but then increased very rapidly at the edge of the cap to maximum values of 100 to 125 pr.-μm in the dark circumpolar region, and then gradually decreased to less than 25 pr.-μm by 60°N [*Davies*, 1982]. The elevated water vapor abundances observed in the north polar region during early summer are generally acknowledged to be due to three factors. The first is that there are abundant water sources on the surface in the form of permanent ice deposits at the residual cap [*Farmer et al.*, 1976] and possibly in the form of seasonal ice deposits in the surrounding area [*Davies*, 1981]. The second is that, because the polar atmosphere does not experience large diurnal temperature variations, its water vapor holding capacity is not limited by nighttime condensation as it is at lower latitudes. The third is that circulation models show that the rate of water transport to lower latitudes is not likely to be very efficient during this season, and that most of the water produced in the polar region remains at high latitudes [*Haberle and Jakosky,* 1990].

A consideration of water ice temperatures and atmospheric water vapor abundances can provide insight into whether the north polar layered terrains could contain stable, near-surface water ice. Table 5 shows basic thermal model calculated daily minimum, maximum and average surface temperatures midway through the mapping period at 80°N for typical regions containing bright water ice deposits, polar layered deposits, and dark circumpolar dunes. The thermal model parameters used are representative of those that provide good fits to the IRTM observations of these regions during this season. Also shown are estimates of the maximum water vapor holding capacity of the Martian atmosphere in these regions, which were determined by assuming the atmosphere was saturated with water at all altitudes.

Table 2. One-Dimensional Model-Calculated Quantities for Eight Model Atmospheres at 60°N and 80°N for I=83.72 and A_s=0.25 from Figure 12

	Latitude 60°N									Latitude 80°N								
	0	1	2	3	4	5	6	7	8	0	1	2	3	4	5	6	7	8
T_{20}min	149.5	169.3	176.2	188.3	190.2	172.4	174.0	170.0	172.8	205.5	215.3	212.4	212.3	214.0	211.3	208.9	212.0	207.5
T_{20}avg	211.2	220.6	219.9	220.4	221.7	219.5	217.6	219.1	217.3	225.9	232.8	229.4	226.2	227.1	229.6	226.3	229.9	225.3
T_{20}max	265.4	266.6	261.7	253.9	253.9	264.4	260.0	264.5	260.7	244.3	248.5	244.9	239.4	239.9	246.3	242.0	246.0	241.4
I^*	84.6	158.7	220.4	360.8	414.3	182.0	203.7	165.4	192.0	84.6	188.7	188.7	278.8	313.8	150.9	162.0	162.0	152.0
A^*	0.25	0.16	0.19	0.22	0.20	0.19	0.22	0.19	0.22	0.25	0.14	0.19	0.23	0.22	0.19	0.24	0.19	0.25
$T_s$min	149.5	169.3	173.4	182.3	183.3	171.1	171.6	169.7	172.1	205.5	215.3	212.8	211.5	211.9	211.1	209.6	212.5	208.8
$T_s$avg	211.2	220.6	221.0	222.8	223.4	219.6	218.9	219.7	219.0	225.9	232.8	231.2	229.2	229.4	230.0	228.4	230.8	227.6
$T_s$max	265.4	266.6	266.3	265.1	265.3	265.7	264.8	265.9	264.8	244.3	248.5	248.0	246.0	246.1	247.1	245.4	247.1	244.5
I_s^*	84.6	158.7	185.4	258.8	272.1	170.4	172.0	162.0	175.4	84.6	188.7	155.4	162.0	172.0	141.6	141.6	158.7	141.6
A_s^*	0.25	0.16	0.16	0.16	0.15	0.18	0.19	0.17	0.19	0.25	0.14	0.17	0.20	0.19	0.19	0.21	0.17	0.22
A_p	0.25	0.25	0.23	0.22	0.21	0.23	0.26	0.25	0.27	0.25	0.25	0.24	0.24	0.23	0.24	0.28	0.27	0.30
T_{15}min	-	170.2	188.5	197.6	181.4	190.3	182.4	175.1	179.2	-	171.8	195.6	208.2	186.9	197.4	187.8	178.0	182.6
T_{15}max	-	171.6	193.6	208.7	184.1	194.3	186.7	177.8	183.9	-	172.2	197.1	211.4	187.7	198.5	189.2	178.9	184.2

Since the IRTM 15-μm channel observations show that atmospheric temperatures at altitudes of ~25 km are only 172 K during this season (see Figure 16), it is clear that the bulk of the water vapor observed by MAWD at this latitude must be concentrated in the lower atmosphere. In accordance with the general results of one-dimensional radiative-convective model simulations, lower atmospheric temperatures were assumed to decrease linearly from the surface to an altitude of 25 km, and were assumed to be isothermal to the "top" of the atmosphere at 50 km. Atmospheric temperatures at the surface were assumed to be equal to the daily averaged temperature of the surface, and atmospheric temperatures at 25 km were assumed to be equal to the measured value of T_{15}. Column water vapor abundances were calculated assuming that the water vapor concentration at each level of the atmosphere was equal to the local saturation vapor pressure. Over regions containing primarily bright water ice deposits, this procedure yields maximum column water vapor abundances of 28.4 pr.-μm, which are in excellent agreement with the MAWD observations. Over regions of layered deposits, the prediction of 106.5 pr.-μm is also in excellent agreement with MAWD. Over the dark dune deposits, the prediction of 403 pr.-μm is much higher than the MAWD observations. The fact that atmospheric water vapor abundances over the north polar layered deposits are consistent with saturation during this season is important, because it leaves open the possibility that they could contain near-surface water ice. However, this is not the only possible explanation. *Haberle and Jakosky* [1990] have performed zonally symmetric circulation model simulations in which evaporation from bright residual water ice deposits is the only source of water vapor in the north polar region during this season. Their results show that the equatorward transport of water vapor off the cap can also lead to large water vapor abundances in the warm region surrounding the cap. Therefore, the possibility of local water vapor transport during this season makes it difficult to trace the original source regions of the observed atmospheric water vapor.

The analysis presented above suggests that if water ice were present within the north polar layered deposits, it might be stable to evaporation during the summer season. Analysis of multispectral Viking orbiter images by *Thomas and Weitz* [1989] shows that the uppermost surface regions in the north polar region that display layering contain patches of exposed ice, as well as materials that have colors and albedos that span the range between those of bright dust deposits in low thermal inertia regions, and the dark circumpolar dune fields. The thermal stability of water ice below dark, low thermal inertia surface soil layers can be investigated using the two-layer thermal model described earlier. Figure 18 shows the results of a set of calculations analogous to those in Figure 17, except that they assume the presence of a soil layer with an albedo of 0.3 and a thermal inertia of 272 J m^{-2} s$^{-1/2}$ K^{-1} overlying material with a thermal inertia of 1000 J m^{-2} s$^{-1/2}$ K^{-1}. The results are similar to those in Figure 17, and imply that if the north polar layered deposits are mantled by an unbonded dust or sand layer, then the thickness of this layer must be less than approximately one-fifth the diurnal skin depth, which is approximately 6 mm for this example. Otherwise, the deposits would have low apparent inertias. It has been suggested in previous studies that the presence of such a soil layer would tend to reduce the amplitudes of subsurface temperature variations and protect underlying ice deposits from sublimation [*Toon et al.*, 1980; *Hofstadter and Murray*, 1990; *Paige*, 1992]. Figure 19 shows calculated diurnal minimum, maximum, and average temperatures at the surface

Table 3. One-Dimensional Model-Calculated Quantities for Eight Model Atmospheres at 60°N and 80°N for I=272 and A_s=0.25 from Figure 13

	Latitude 60°N									Latitude 80°N								
	0	1	2	3	4	5	6	7	8	0	1	2	3	4	5	6	7	8
T_{20}min	179.5	190.5	193.4	199.8	201.3	191.6	191.5	190.1	190.7	211.4	219.7	216.8	215.6	216.9	216.2	213.5	216.7	212.2
T_{20}avg	217.6	224.6	223.0	222.1	223.1	223.1	220.8	222.9	220.6	225.2	232.0	228.6	225.2	226.2	228.8	225.4	229.1	224.4
T_{20}max	254.7	257.5	253.0	246.3	246.8	255.1	250.9	255.3	251.6	238.4	243.5	239.9	234.8	235.4	240.9	236.8	240.9	236.1
I*	287.1	404.2	477.7	645.1	693.4	430.9	454.3	408.5	437.6	287.3	431.0	427.6	557.6	604.3	367.5	387.5	390.8	357.5
A*	0.25	0.16	0.19	0.21	0.20	0.18	0.22	0.19	0.22	0.25	0.14	0.19	0.23	0.21	0.19	0.24	0.19	0.25
$T_s$min	179.5	190.5	192.6	197.8	198.8	191.0	191.0	190.3	191.2	211.4	219.7	217.7	216.1	216.4	216.2	214.7	217.3	213.9
$T_s$avg	217.6	224.6	224.6	225.4	225.9	223.4	222.7	223.7	222.7	225.2	232.0	230.4	228.2	228.4	229.1	227.6	229.9	226.7
$T_s$max	254.7	257.5	257.0	255.7	255.8	256.2	255.2	256.6	255.3	238.4	243.5	242.6	240.3	240.3	241.5	239.8	241.9	239.0
I_s*	287.1	404.2	434.3	527.6	547.6	411.8	414.3	401.8	417.6	287.3	431.0	375.8	389.2	407.5	347.5	337.4	384.2	334.1
A_s*	0.25	0.16	0.16	0.16	0.15	0.18	0.19	0.17	0.19	0.25	0.14	0.17	0.20	0.19	0.19	0.21	0.17	0.22
A_p	0.25	0.25	0.23	0.22	0.21	0.23	0.26	0.25	0.27	0.25	0.25	0.24	0.24	0.23	0.24	0.28	0.27	0.30
T_{15}min	-	169.2	188.5	198.1	181.2	190.1	182.3	174.6	179.1	-	171.1	195.3	208.0	186.6	197.2	187.3	177.3	182.0
T_{15}max	-	170.5	192.9	207.7	183.6	193.7	185.9	176.8	182.6	-	171.5	196.5	210.5	187.3	198.1	188.4	178.1	183.2

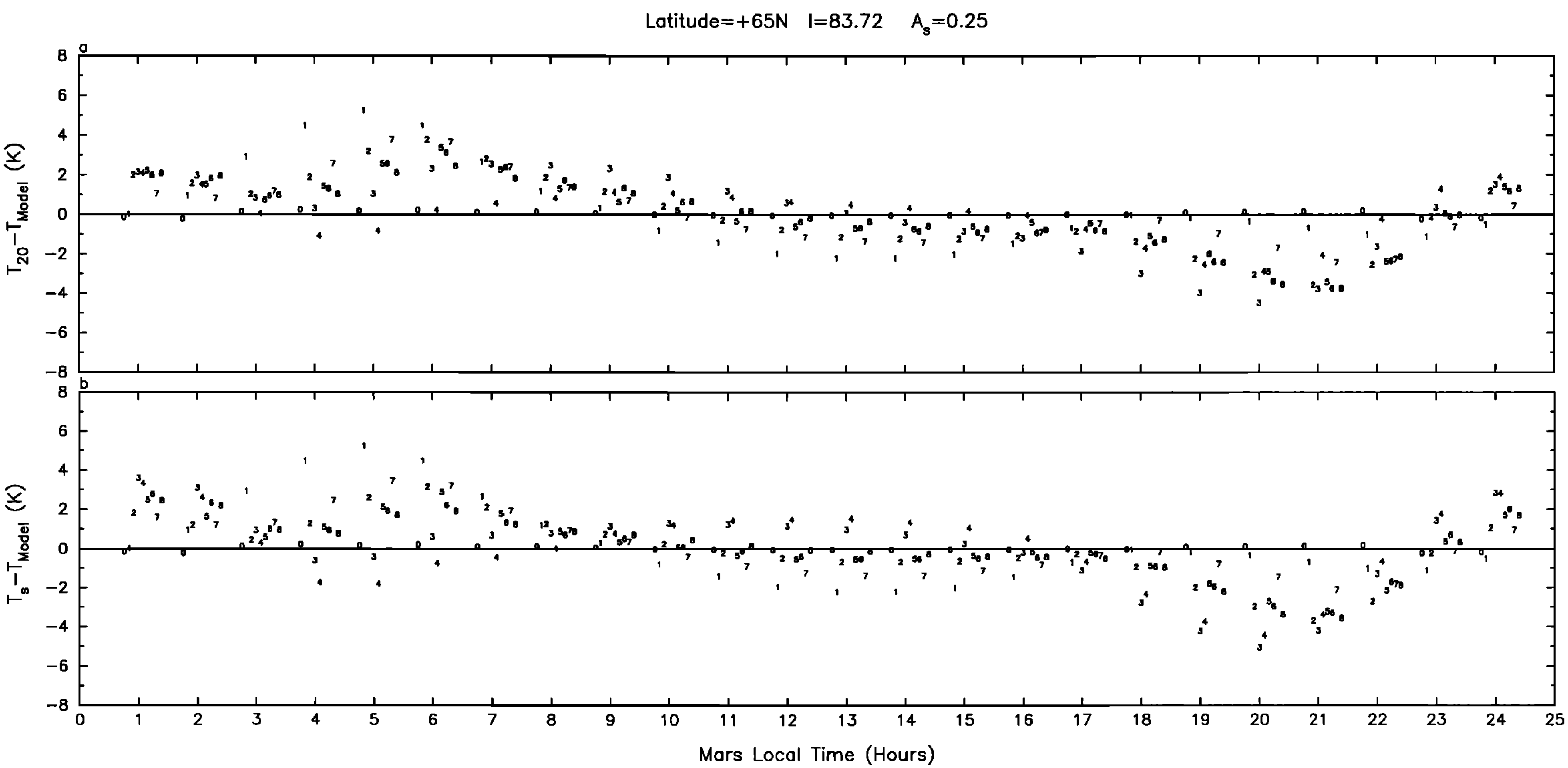

Figure 14. Computed residual diurnal variability due to the effects of the atmosphere. (a) Differences between one-dimensional model-calculated IRTM 20-μm channel brightness temperatures at the top of the atmosphere T_{20} and best fit basic thermal model temperatures T_{Model} as a function of Mars local time at 60°N. Numeric symbols represent the results for the corresponding model atmospheres in Table 1. The symbols are offset horizontally from their true Mars local times, which assume integer values. (b) Same as Figure 14a, except for one-dimensional model-calculated surface temperatures instead of one-dimensional model-calculated brightness temperatures.

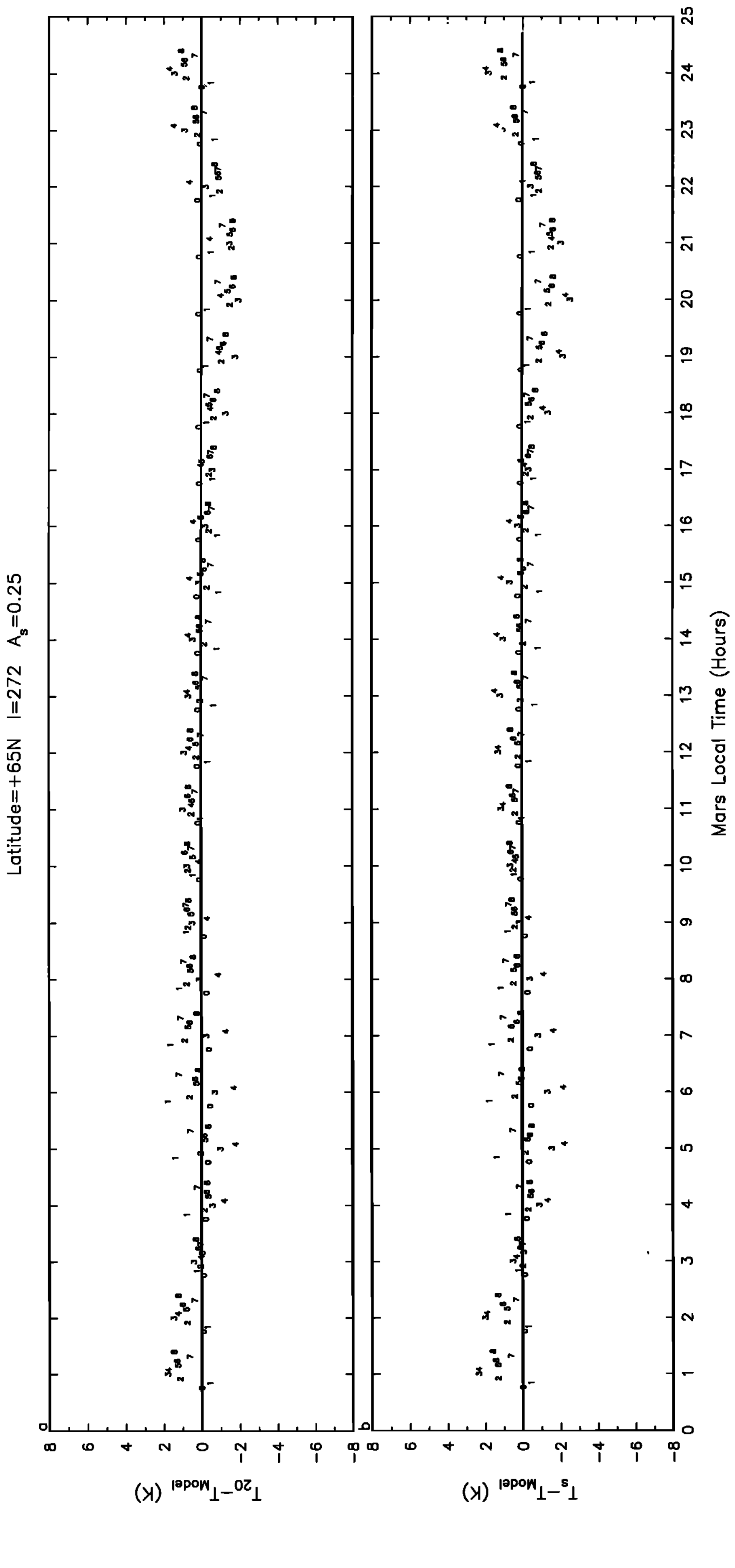

Figure 15. Same as Figure 14 assuming a surface thermal inertia of 272 J m^{-2} s$^{-1/2}$ K^{-1}.

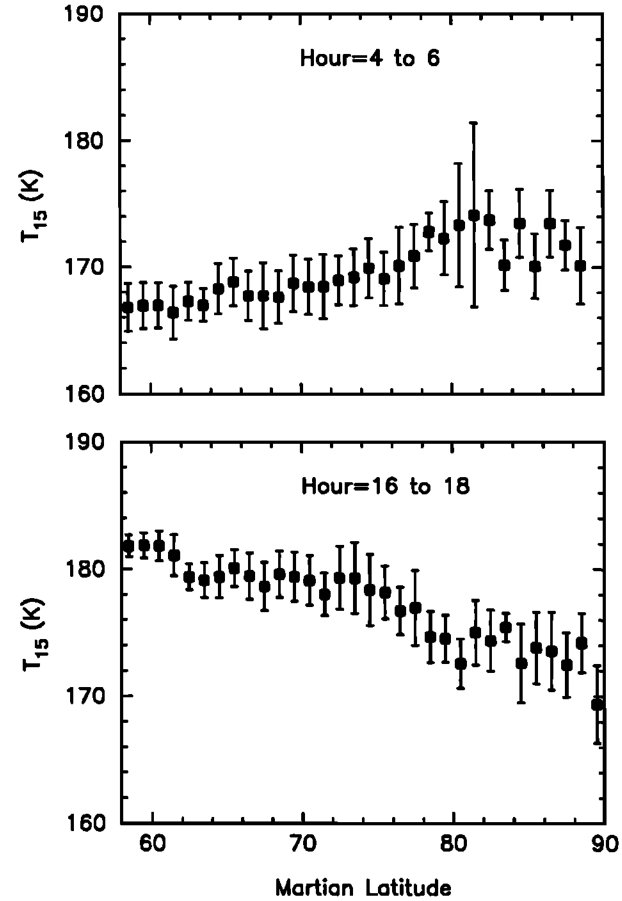

Figure 16. Latitudinally averaged IRTM 15-μm channel brightness temperatures with standard deviations. Plotted are all observations obtained for emission angles of less than 60° between (a) 4 and 6 hours and (b) 16 and 18 hours.

and at the uppermost high thermal inertia ice layer for the same two-layer model cases shown in Figure 18. As would be expected, if ice is close enough to the surface to be responsible for the high apparent thermal inertias of these terrains, then the degree of thermal protection it would receive from a thin overlying soil layer would be small.

The results in Figure 19 may also provide some insight into feedback processes that could potentially lead to the stability of water ice in such close proximity to the surface. *Paige* [1992] has shown that at lower latitudes, the process of ground ice formation below low thermal inertia surface soil layers is thermally stable, and can be enhanced by the thermal effects of the high thermal inertia ice deposits themselves. At high latitudes, the feedback processes demonstrated in *Paige's* [1992] study are also expected to occur. In the north polar region, the abundance of near-surface atmospheric water vapor during the summer season is determined by the saturation vapor pressure, which is in turn determined by the temperature of the surface itself. Figure 19 shows that daily-averaged surface soil temperatures are completely unaffected by the presence of near-surface ice, which means that to first order, near-surface frost-point temperatures are independent of the presence of ice within the layered deposits as long as there are sources of water vapor in the general vicinity. If the average surface frost-point temperature is fixed, then sublimation within ice-saturated layers at depth would result in an increase in the depth of the overlying unfrosted surface soil layer and lower subsurface ice temperatures, which would result in the recondensation of water at depth and tend to restore ice to its original level below the surface. As long as near-surface frost-point temperatures near the pole are close to actual surface temperatures, then the equilibrium thicknesses of any low thermal inertia surface soil layers near the pole, if present at all, would be expected to be very small.

When considering the stability of water ice in the north polar layered deposits over long timescales, the effects of horizontal water vapor transport and erosion and deposition must also be considered. Both issues are difficult to address with presently available observations. Although there can be little question that there is a net transport of water vapor away from the north polar region during the summer season [*Farmer et al.*, 1976; *Farmer and Doms*, 1979; *Davies*, 1981; *Jakosky and Farmer*, 1982; *Haberle and Jakosky*, 1990], there is a distinct possibility that at least some of this water may be transported back to the polar region from lower latitudes during other seasons [*Davies*, 1981; *Barnes*; 1990; *Santee*, 1992]. This situation is further complicated by the heterogeneous nature of the various polar terrains, and there may be significant local redistribution of water from dark regions to bright regions [*Kieffer et al.*, 1976a]. Despite these many uncertainties, the results of this study show that the north polar layered deposits have high thermal inertias, which suggests very strongly that they contain near-surface ice

Some of the most intriguing clues to the properties of the north residual cap and the north polar layered deposits come from observations of temporal variations in bright water frost coverage. *James and Martin* [1985] have reported that moderately high resolution Viking Orbiter images of the Chasma Boreal region and the central region of the cap show less frost coverage at L_s 118 in 1978 than Viking Orbiter images obtained nearly one Mars year earlier at L_s 135 in 1976. *Kieffer* [1990] has also reported the nearly complete disappearance of a detached bright frost deposit near Chasma Boreal at 82°N, 44°W between L_s 134 in 1976, and L_s 110 in 1978. Figure 20 shows a Mariner 9 wide-angle camera image of north residual cap region obtained in 1972 at L_s 110, which was processed by M. C. Malin (personal communication; 1993). Comparison between this

Table 4. Estimates for Expected Variation in Thermal Inertia

Material	Estimated Mean Effective Particle Diameter, μm	Thermal Inertia, MKS	Source
Mars dust	5	40	*Haberle and Jakosky* [1991]
Mars silt	50	125	*Edgett and Christensen* [1991]
Mars fine sand	200	230	*Edgett and Christensen* [1991]
Mars coarse sand	700	375	*Edgett and Christensen* [1991]
Terrestrial sandstone	-	2344	*Carslaw and Jaeger* [1959]
Mars solid ice	-	2045	*Kieffer* [1990]

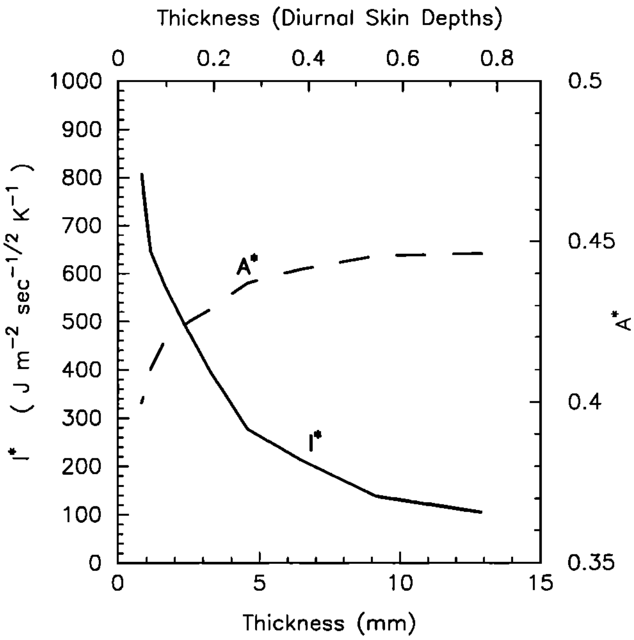

Figure 17. Best fit apparent thermal inertias I^* and best fit apparent albedos A^* as for a series of two-layer thermal model calculations in which a series of thin, low inertia surface layers with I=100 J m^{-2} s$^{-1/2}$ K^{-1} of different thicknesses were assumed to overlie a semi-infinite, high thermal inertia layer with I=1000 J m^{-2} s$^{-1/2}$ K^{-1}. Thicknesses of the upper low thermal inertia layer are given in millimeters, and in diurnal skin depths within the upper layer. The calculations were performed at 80°N midway through the mapping period at L_s 110 assuming a surface albedo of 0.4, and a product ρc of 1 x 10^6 J m^{-3} K^{-1} at all depths.

image and the Viking photomosaic shown in Figure 10, which was obtained more than three Mars years later, reveals striking differences in the amount of bright frost coverage. The Mariner 9 image shows distinctly less frost coverage, particularly in the outer portions of the cap. Examination of the images shows that these differences are not artifacts of the different image processing techniques used to create these images. One of the most convincing changes occurs at 86°N, 60°W, where the Viking images show the connection of a bright frost band that is clearly not connected in the Mariner 9 image. The fact that the albedos of these areas can change so dramatically over such short timescales suggests that thin seasonal surface layers of ice-rich or dust-rich material were deposited or removed. *James and Martin* [1985] favored the hypothesis that the reduced frost coverage observed in 1978 relative to 1976 was due to dust deposition which occurred during the two global dust storms of 1977. The even more reduced frost coverage shown in the Mariner 9 image, which was obtained after the even more severe global dust storm of 1971-1972, is consistent with this pattern. The large interannual variations in residual north polar cap frost coverage suggested by these spacecraft observations may also be related to a curious telescopic feature known as the Rima Tenuis [*Capen*, 1980]. First observed by Schiaperrelli in the 1880s, the Rima Tenuis is a dark fissure along the 150°W-330°W meridian that appears to divide the north residual cap into two unequal parts. The feature has since been observed A. E. Douglass at the Lowell Observatory in 1901, and photographed by the members Association of Lunar and Planetary Observers in 1980 [*Capen*, 1980]. Apparently, the Rima Tenuis is visible only during summer seasons when the north residual cap is unusually small.

When taken as a whole, the observations presented in this paper suggest that in future studies, the north polar bright ice deposits, and the exposed north polar layered deposits might best be considered as a single entity. The fact that extensive regions which appeared dark during the summer season of 1972 appeared bright and had high thermal inertias in 1978 suggests two possible explanations. The first is that a thin layer of dark, dust-rich material was removed from these regions of the cap between 1972 and 1976. The second is that a thin layer of bright, ice-rich material was deposited during the same period. Of the two, the second hypothesis seems the more likely, given that the removal of a dark surface dust deposit is not likely to leave a completely clean, bright, dust-free surface. If a widespread bright, ice-rich surface layer did form between 1972 and 1976, and it did not sublimate completely, then the Mariner 9 and Viking observations could potentially be interpreted as fragmentary evidence for the ongoing formation of layered deposits in the north polar region over interannual timescales.

North Polar Dune Deposits

The dark north circumpolar dune deposits are the most extensive dune deposits on the planet. Their morphology, distribution, and spectral properties have been addressed in a number of previous studies [*Cutts et al.*, 1976; *Breed et al.*, 1979; *Tsoar et al.*, 1979; *Tanaka and Scott,* 1987; *Thomas and Weitz,* 1989; *Lancaster and Greeley*, 1990; *Thomas et al.*, 1992]. Within the dune deposits, both barchan and transverse dune forms are observed. In most regions, the areal coverage of dune material is not complete. Figure 21 shows a map compiled by *Lancaster and Greeley* [1990] which shows contours of the percentage of transverse and barchan dune cover observable in the available Viking imagery of the north polar region. *Thomas and Weitz* [1989] have shown that the spectral reflectance properties of the north polar dunes within the Viking Orbiter red, green and violet filter passbands are very similar to those observed for low-latitude intracrater dune deposits in the northern and southern hemispheres. The Viking Orbiter images also show clear evidence for the transport of dune material away from

Table 5. Surface Temperatures and Water Vapor Abundances at 80°N

Surface	Surface Albedo	Thermal Inertia, MKS	Daily Minimum Surface Temperature, K	Daily Maximum Surface Temperature, K	Daily Average Surface Temperature, K	Estimated Saturated Column Water Vapor Abundance, pr.-μm
Ice	0.4	1150	204.22	212.93	208.58	28.4
Layered terrain	0.3	535	211.24	228.98	220.18	106.5
Dunes	0.15	225	216.70	248.12	232.81	403.5

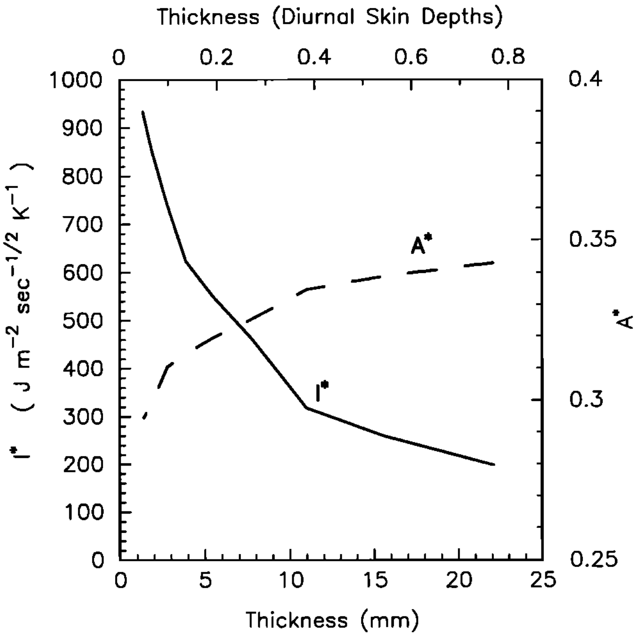

Figure 18. Same as Figure 17 for a surface layer with I=272 J m^{-2} s$^{-1/2}$ K^{-1} and A_s=0.3.

arcuate scarps within the layered deposits [*Tsoar et al.*, 1979; *Thomas and Weitz*, 1989], and it is generally acknowledged that the polar layered deposits are a source for much of the circumpolar dune material [*Thomas et al.*, 1992]. This hypothesis is supported by observations showing that certain portions of the polar layered deposits contain materials that have color ratios that are similar to the dune deposits themselves [*Thomas and Weitz*, 1989].

One of the most interesting results of this study is that portions of the north circumpolar dune deposits have low thermal inertias. Plate 7 indicates that within regions classified by *Tsoar et al.* [1979] as transverse dunes, there are extended areas which have apparent thermal inertias of 150 J m^{-2} s$^{-1/2}$ K^{-1} or lower. The largest of these areas occurs between 120°W and 210°W, which corresponds quite closely to the largest region with 100% dune cover mapped by *Lancaster and Greeley* [1990] (see Figure 2). The average thermal inertias of the 38 mapping regions completely within the *Lancaster and Greeley* [1990] 100% dune coverage areas is 192 J m^{-2} s$^{-1/2}$ K^{-1}. Moderately low thermal inertia material also appears to be present at the location of an arcuate scarp within the polar layered deposits at 84.5°N, 125°W, which appears to be a major source region for the largest transverse dune deposit [*Tsoar et al.*, 1979; *Thomas and Weitz*, 1989], although higher-resolution data are required to resolve this feature. Regions that contain barchan dunes, which tend to have much less than 100% dune cover, typically have higher thermal inertias than the more completely covered transverse dune regions. This may be consistent with the notion that the barchan dunes also consist of lower thermal inertia material, but that the IRTM observations of these regions are affected by the presence of exposed higher-inertia polar plains material that underlies the dunes. The regions within the dark circumpolar area that have some of the highest apparent thermal inertias, such as those between longitudes of 320°W to 360°W, occur in areas that are not mapped as containing dunes. These areas may be analogous to dark, high thermal inertia intracrater deposits observed at lower latitudes [*Christensen*, 1983].

The apparent thermal inertias of the north polar dune deposits appear to be distinctly lower than dune deposits elsewhere on the planet. *Edgett and Christensen* [1991] have analyzed IRTM brightness temperature observations of four continuous intracrater dune deposits at lower latitudes, and found them all to have apparent thermal inertias between 330 and 356 J m^{-2} s$^{-1/2}$ K^{-1}, which according to the estimates summarized in Table 4, implies average effective particle diameters on the order of 500 μm. Since dunes, which are formed by saltation, are generally composed of a narrow range of particle sizes, they are considered to be good surfaces to test theories of particle size-conductivity relationships and aeolian transport in the Martian environment. *Edgett and Christensen* [1991] have applied the aeolian transport theories of *Iverson and White* [1982], *Greeley and Iverson* [1985], and *White* [1979], and have found that under present Martian atmospheric conditions, the crystalline materials with particle diameters of greater than ~210 μm are expected to be transported by saltation, whereas crystalline materials with particle diameters of less than ~210 μm are expected to be transported by suspension. *Edgett and Christensen* [1991] interpreted their inferred effective dune particle diameters of ~500 μm as being consistent with the predictions of aeolian transport theory.

We have identified three possible explanations for the low apparent thermal inertias of dark dune deposits in the north polar region. The remainder of this section consists of a description of these three explanations, followed by a short discussion.

The effects of the atmosphere. The first explanation involves the effects of the atmosphere. In the last section, it was demonstrated that at both high and low latitudes, measured apparent thermal inertias are only upper limits for actual thermal inertias during this season. Even assuming low or zero aerosol

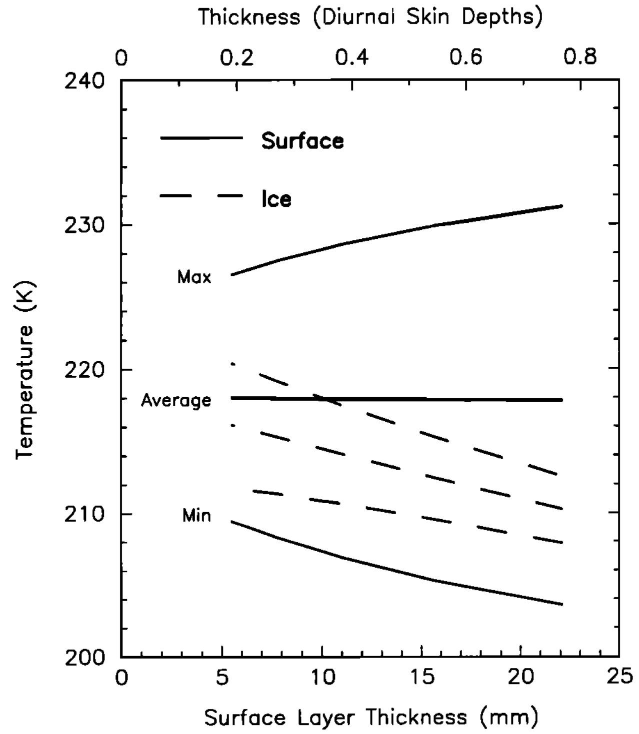

Figure 19. Diurnal minimum, maximum, and average temperatures at the surface, and at the top of the high thermal inertia ice layer as a function of surface soil layer thickness for the same series of two-layer model cases shown in Figure 18.

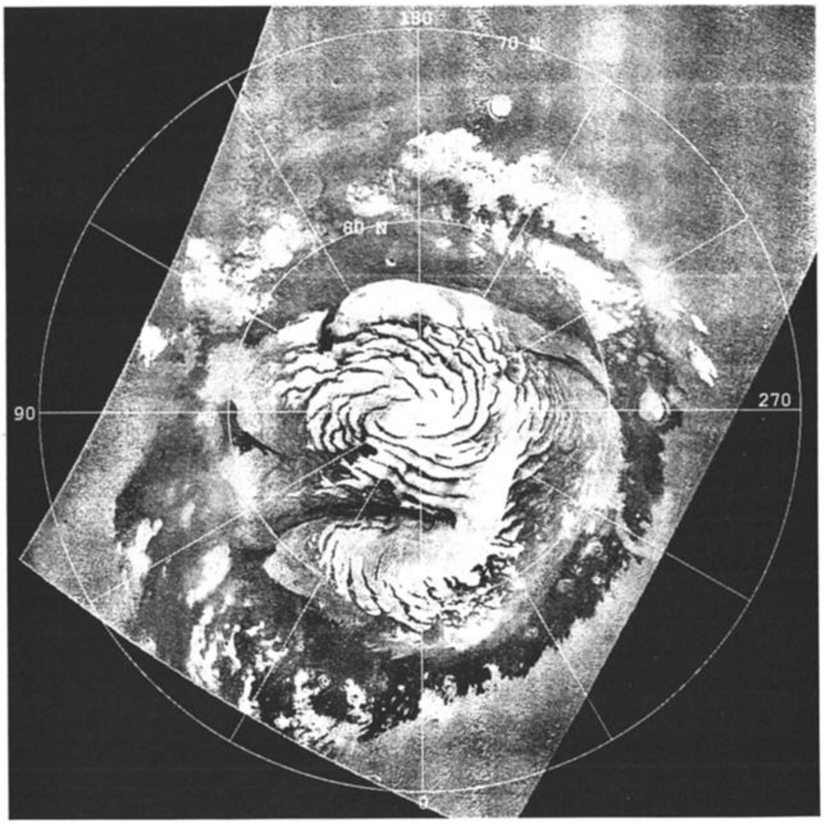

Figure 20. A Mariner 9 wide-angle camera image of the polar region of Mars, obtained at L_s 101 in 1972 (DAS 13317550), which was processed by M. C. Malin (personal communication 1993) This image was acquired three Mars years before the Viking image shown in Figure 10. The raw image was corrected for dropped lines and bit errors, high-pass filtered over a 101 by 101 pixel window to remove photometric shading, refiltered with high-pass and low-pass filters using weighting factors of 0.8 and 0.2 over 3 by 3 pixel windows to emphasize albedo variations, and then stretched and geometrically rectified to create a polar stereographic map.

opacity, the results presented in Figures 12 and 13 would imply that the actual thermal inertias of the polar dune deposits must be lower than their measured apparent thermal inertias by at least 100 J m^{-2} s$^{-1/2}$ K^{-1}. If this were true, then standard particle size-conductivity relationships would imply mean effective particle diameters of the dune particles on the order of 50 μm, and standard aeolian transport theory would imply that crystalline particles in this size range would be transported more by suspension than saltation under present atmospheric conditions. One way to partially reconcile this apparent discrepancy would be to propose that dunes in all areas of the planet have similar actual inertias, but that the effects of the atmosphere on apparent inertias are greater at lower latitudes.

Table 5 shows the results of a series of one-dimensional model calculations that are designed to further illustrate the effects of the atmosphere on determinations of apparent thermal inertia. The calculations were performed at 48°S at L_s 20, which are the approximate latitude and season of many of the dune observations in the *Edgett and Christensen* [1990] paper. Shown in Table 5 are computed surface temperatures T_s and IRTM 20-μm channel brightness temperatures T_{20} for surface thermal inertias of I=150 and 350 J m^{-2} s$^{-1/2}$ K^{-1}. Model atmosphere A uses the 2% assumption of *Kieffer et al.* [1977]. Model atmosphere B assumes a 7-mbar CO_2 atmosphere with no aerosols. Model atmosphere C assumes a 7-mbar CO_2 atmosphere and Mariner 9-inferred dust distributed uniformly with pressure, with a solar spectrum average dust optical depth of 0.2. Model atmosphere D is the same as C, but the solar spectrum average dust optical depth is 0.6. Also shown in Table 6 are single-point thermal inertia determinations computed in a manner analogous to that used by *Edgett and Christensen* [1990]. Because of the unavailability of daytime observations, *Edgett and Christensen* [1990] used a simplified "single-point" method for determining thermal inertias in which measured brightness temperatures obtained during the predawn hours are compared to a set of thermal model calculations which assume a fixed surface albedo. *Edgett and Christensen* [1990] employed the *Kieffer et al.* [1977] thermal model which assumes a constant surface heating rate of 2% of the local noontime insolation, and assumed that the surface albedo was 0.15 for all cases. Table 6 shows an analogous set of single-point thermal inertias at 0 hours local time using the computed surface temperatures ISP_s, and the computed IRTM 20-μm channel brightness temperatures at the top of the atmosphere *ISP*. For Model atmosphere A, the two types of calculated single-point inertias are identical to the inputs. For Model atmosphere B, the two types of calculated single-point inertias are equal, but higher than the inputs. For Model atmospheres C and D, both types of calculated single-point inertias are higher than the inputs. For C and D, *ISP* is higher than ISP_s because the atmosphere is warmer than the surface, which causes T_{20} to be higher than T_s. The results shown in Table 6 indicate that the actual thermal inertias of midlatitude

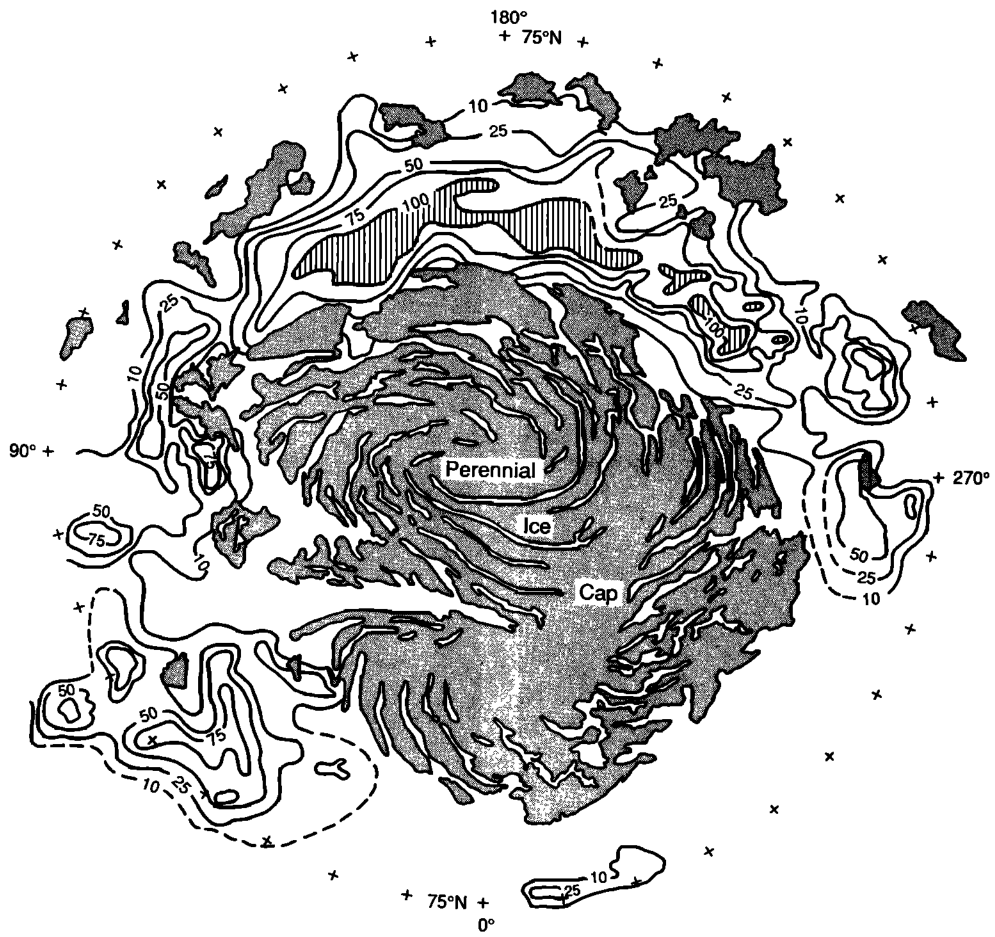

Figure 21. Contours of percentage cover of dunes in the north polar region visually estimated over areas of approximately 100 km^2 using Viking Orbiter images [from *Lancaster and Greeley*, 1990].

dune materials may be considerably lower than suggested by Edgett and Christensen's analysis. More generally, they provide additional evidence that without independent information concerning the spatial and temporal distribution of atmospheric aerosols and their optical properties, it is not possible to determine the absolute thermal inertias of most Martian surface materials in a unique manner from remote observations.

The effects of dune surface slopes. A second explanation for the low thermal inertias of north polar dune deposits is that they are due to the effects of dune surface slopes. From a morphologic standpoint, the dune regions that have the lowest apparent inertias contain regularly spaced transverse dunes oriented perpendicularly to predominantly northeast to southwest winds [*Tsoar et al.*, 1979]. Dune face profiles in this region tend to be more symmetric than in other locations, suggesting a seasonal 180° reversal in wind direction [*Tsoar et al.*, 1979], which would also explain why aeolian material has accumulated in these areas [*Lancaster and Greeley*, 1990]. The effects of rough surfaces and topographic relief on the thermal emission of planetary surfaces have been investigated in a number of contexts. For this study, we have developed a relatively simple model to assess the potential effects of dune slopes on apparent thermal inertia measurements. In accordance with most of the Viking Orbiter imaging observations of these regions, the dunes are assumed to have regular "washboard" topographic profiles, with the possibility of unequal slope angles on the upwind and downwind faces. Surface temperatures for both dune faces are calculated using a modified version of the basic thermal model described earlier. Direct insolation rates for each dune face are determined independently, accounting for the direction and angles of the slope normals and the local horizon, but not accounting for possible shadowing by adjacent dune faces. Indirect insolation rates for each dune face are also determined independently during each model time step, accounting for direct solar radiation reflected from the opposite dune face, but not accounting for other possible sources of indirect illumination such as multiple reflections and scattered skylight. The indirect insolation rates are determined geometrically at the midpoints of slopes assuming Lambertian bidirectional reflectance functions. The model also accounts for infrared heating rates due to the presence of adjacent dune slopes, which are determined geometrically at the midpoints of slopes assuming that all surfaces are blackbody emitters with unit emissivity. Once the temperatures of both dune slopes have been determined, IRTM 20-μm channel brightness temperatures are calculated for normal viewing geometry using the projected area-weighted Planck functions of the dune faces and the spectral response of the IRTM 20-μm channel. For all cases, the dune materials are assumed to have thermal inertias of 272 J m^{-2} $s^{-1/2}$ K^{-1} and surface albedos of 0.15.

Figure 22 shows calculated diurnal surface temperature variations for individual dune slopes at 60°N and 80°N, midway

Table 6. Single-Point Thermal Inertias at Midnight, 48°S, L_s=20

	I=150 MKS A_s=0.15				I=350, MKS A_s=0.15				
Atmosphere	T_s	ISP_s	T_{20}	ISP	T_s	ISP_s	T_{20}	ISP	Comment
A	157.8	150	157.8	150	175.0	350	175.0	350	2% atmosphere
B	163.3	195	163.3	195	177.6	407	177.6	407	CO_2 atmosphere
C	164.6	207	165.9	222	177.6	407	177.7	409	τ_{so}=0.2
D	167.4	238	170.2	273	178.4	427	178.9	439	τ_{so}=0.6

through the mapping period at Julian date 2443695 (L_s 109.86). For these examples, the dunes were assumed to have symmetric profiles, with 20° slopes on both the upwind and downwind faces. The figures show daily temperature variations for north, south, east, and west facing slopes compared with those expected for flat surfaces with the same thermophysical properties. Figure 23 shows calculated IRTM 20-μm channel brightness temperatures for dune fields with the same 20° symmetric slope profiles at 60°N and 80°N. Tables 7 and 8 show best fit apparent thermal inertias I^* and best fit apparent albedos A^* for the dune field brightness temperatures in Figure 23 using the basic thermal model, which assumes that no slopes are present. Relatively speaking, dune slopes have much larger effects on apparent thermal inertias at 80°N than they do at 60°N during this season. To our knowledge, there are no direct measurements of the

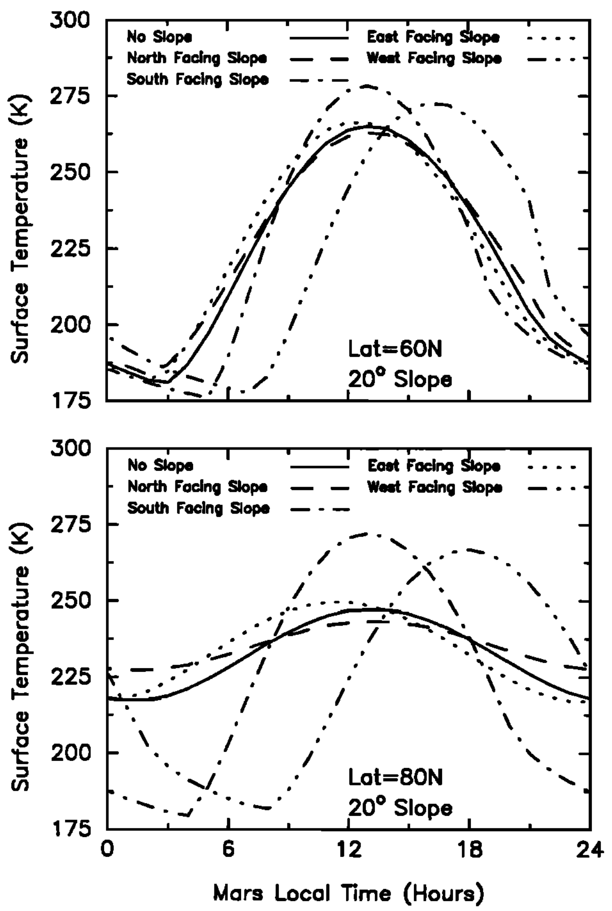

Figure 22. Calculated daily surface temperature variations for symmetric dune faces with 20° slopes at 60°N and 80°N midway through the mapping period. All surfaces are assumed to have I=272 J m^{-2} s$^{-1/2}$ K^{-1} and A_s=0.15.

angles of the Martian dune slopes. *Lancaster and Greeley* [1990] have estimated that the ratios between the dune peak heights to dune spacing for Martian transverse dunes should be on the order of 1:22 based on terrestrial analogs. If this were true, then actual slope angles for transverse dunes with symmetric slope profiles would be only ~4°, and actual slope angles for dunes with asymmetric slope profiles would be ~3° for upwind slope faces, and an average of ~20° for downwind slope faces. Tables 7 and 8 also show best fit apparent thermal inertias and albedos for these more shallow symmetric and asymmetric dune slope profiles at 60°N and 80°N. If actual dune slopes are as shallow as 4°, their effects on thermal inertia could be considered negligible at both latitudes.

If slopes have significant effects on dune brightness temperatures, then the IRTM observations would be expected to show unique patterns of residual diurnal variability. Figure 24 (top) shows calculated differences between selected dune slope model-calculated IRTM 20-μm channel brightness temperatures and best fit basic thermal model temperatures as a function of Mars local time at 80°N for continuous dune fields with slope normals oriented in north-east to south-west directions. Figure 31 (bottom) shows differences between measured IRTM 20-μm channel brightness temperatures and best fit basic thermal model temperatures for regions with I^* < 300 J m^{-2} s$^{-1/2}$ K^{-1} from 78°N to 83°N and 130°W to 205°W. This corresponds to the largest area of complete dune cover in the polar region [*Lancaster and Greeley*, 1990]. As can be seen in the figure, the IRTM observations of this area contain little evidence for unusual diurnal variability, which would imply that the low apparent thermal inertia of this region is not due to the effects of steep dune slopes.

Low thermal inertia particles. A third explanation for the low thermal inertias of north polar dune deposits is that they are composed of low thermal inertia particles. The literature contains a number of interesting ideas on this subject. One suggestion is that the dune deposits are composed of low-density, sand-sized aggregations of smaller particles. Suggested analogs for this material have included irregularly shaped cemented dust and sand fragments called parna [*Greeley*, 1986], or filamentary sublimate residue particles, which can be formed by the complete sublimation of mixtures of ice and silicate dust [*Saunders et al.*, 1986; *Saunders and Blewett*, 1987]. Although the thermal inertias of surfaces composed of such materials would be difficult to predict, they are likely to be significantly lower than those for surfaces composed of crystalline sand [*Herkenhoff*, 1992]. The expected particle sizes of dunes composed of these low-density particles can be estimated using aeolian transport theory. If the *Iverson and White* [1982] formulations for threshold friction velocity based on wind tunnel experiments with "instant tea" particles with densities of 0.21 g cm^{-1} under Martian atmospheric conditions are used, the minimum threshold friction velocity would be expected to be only 0.89 m s^{-1} for particles with

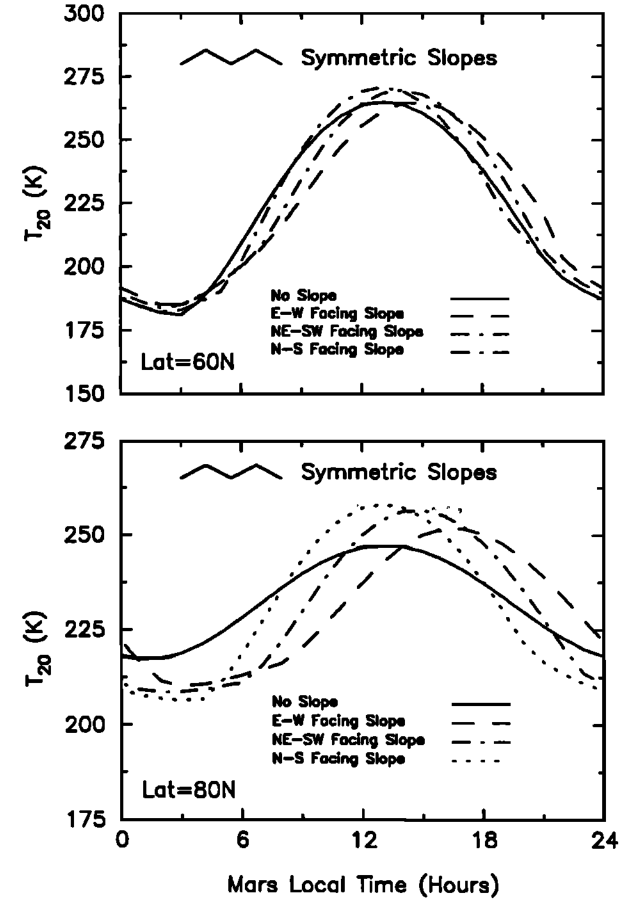

Figure 23. Calculated IRTM 20-μm channel brightness temperature at normal viewing geometry as a function of Mars local time for regions consisting exclusively of symmetric dunes with 20° slopes at 60°N and 80°N midway through the mapping period. All surfaces are assumed to have I=272 J m^{-2} s$^{-1/2}$ K^{-1} and A_s=0.15.

diameters of 330 μm. For particles with these densities, the terminal fall velocity exceeds the threshold friction velocity for all particles with diameters of 510 μm or greater. This implies that the diameters of dune-forming low-density aggregates might be expected to be measured in millimeters. Another possibility that may deserve consideration is that the north polar dunes are composed of very fine grained granular materials that achieve mobility by saltation only when they are surrounded by, or attached to, larger particles that contain seasonal water ice or CO_2 frost. Redistributing dust in this manner was mentioned by *Kieffer* [1990] as a mechanism for explaining observed interannual variations in the albedo of the north residual polar cap.

One serious difficulty with the notion that the north polar dunes are composed of aggregations of low thermal inertia particles is that at low-latitude, low thermal inertia regions generally have high albedos [*Palluconi and Kieffer*, 1981] and high red to violet reflectance ratios [*Thomas and Veverka*, 1986], whereas low-latitude dark intracrater deposits have high thermal inertias [*Christensen*, 1983] and lower red to violet reflectance ratios [*Thomas and Veverka*, 1986]. If the north polar dune deposits were composed of aggregations of low thermal inertia materials, one might also expect them to have color ratios that were similar to those of low thermal inertia regions at lower latitudes [*Thomas and Weitz*, 1989]. Instead, their reflectance properties are essentially identical to those of the dark intracrater deposits [*Thomas and Weitz*, 1989]. *Christensen's* [1983] analysis of Viking and Mariner 9 observations of the dark intracrater deposits shows that they display a wide range of apparent thermal inertias. Only a small percentage of these deposits have recognizable dune forms in the available imagery, and those that do tend to have the lowest apparent thermal inertias [*Christensen*, 1983]. Most of the dark intracrater deposits show no evidence for dune formations, and therefore have been suggested to be composed of very coarse, high inertia material that is transported by creep induced by the impact of aeolian materials [*Christensen*, 1983]. The fact that these deposits are generally associated with topographic obstacles, and that they are not generally found in bright, low thermal inertia regions supports the notion that the mobility of this material is extremely limited [*Christensen*, 1983]. If the dark intracrater deposits contain particles with large and intermediate grain sizes, then it is likely that particles with smaller grain sizes, but similar composition, also exist. Since the finest dark material is likely to be transported by suspension, it should be thoroughly mixed with fine bright material and distributed over much of the planet. This notion is supported by analyses of Viking lander sky brightness measurements, which show that small amounts of a dark mineral such as magnetite may be the principal opaque component of Martian aerosols [*Pollack et al.*, 1977], and by the Viking lander magnetic properties experiment results, which show that dark magnetic mineral grains are present in Martian soil [*Hargraves et al.*, 1979]. While granular deposits composed of the extremely fine grained material presently suspended in the Martian atmosphere would not be expected to form dune deposits under present climatic conditions, there is likely to be a range of dark material with intermediate grain sizes that can be effectively

Table 7. The Effects of Dune Slopes at 60°N

Slope 1 Angle, deg	Slope 1 Normal Direction	Slope 2 Angle, deg	Slope 1 Normal Direction	I*, MKS	A*	σ*
0	-	0	-	268.8	0.145	0.27554
20	N	20	S	252.1	0.135	3.66703
20	E	20	W	344.2	0.160	8.95939
20	NE	20	SW	300.7	0.139	6.50889
10	NE	30	SW	285.5	0.147	3.62219
3.7	NE	3.7	SW	268.8	0.145	0.33140
2.9	NE	20	SW	271.2	0.145	0.86588

Table 8. The Effects of Dune Slopes at 80°N

Slope 1 Angle, deg	Slope 1 Normal Direction	Slope 2 Angle, deg	Slope 1 Normal Direction	I^*, MKS	A^*	σ^*
0	-	0	-	265.5	0.144	0.07954
20	N	20	S	66.9	0.180	6.26114
20	E	20	W	544.5	0.160	10.90878
20	NE	20	SW	168.7	0.180	9.60116
10	NE	30	SW	404.2	0.141	2.55343
3.7	NE	3.7	SW	265.5	0.146	0.09181
2.9	NE	20	SW	275.5	0.150	0.30279

transported by suspension under favorable circumstances, and by saltation the rest of the time.

Discussion. While all three of the explanations we have presented here may be partially responsible for the low apparent thermal inertias of the north polar dune deposits, the hypothesis that these deposits are composed of dark crystalline sand particles seems to us to be the most plausible. It provides a simple explanation for the similarities between the observed color properties of the polar dune deposits and those at lower latitudes [*Thomas and Weitz,* 1989], and is consistent with the observed tendency for dark, dune-forming deposits to have lower thermal inertias than dark, non-dune-forming deposits *Christensen* [1983]. This hypothesis does not require unique or exotic processes for the formation of the north polar dune particles, but it does leave open the question of how this material became incorporated into the polar layered deposits.

One possibility is that these particles were transported to the poles by suspension during periods of high obliquity, when atmospheric pressures may have been significantly higher than today. Another possibility is that these particles were created locally in the vicinity of the residual cap. [*Budd et.al.,* 1986] and *Clifford* [1987] have independently suggested that the Martian polar caps may actually be active continental-scale ice sheets, which balance ice accumulation at their centers with ice ablation at their margins. For this to occur would require that temperatures at the base of the polar caps be warm enough to permit viscous flow, which in turn, would depend on depths and thermal properties of the polar deposits, the rate of heat flow from the Martian interior, and the rate of frictional heat generation due to basal sliding. Unfortunately, none of these quantities are well constrained by presently available observations, and none of the features visible in orbiter images of the surfaces of the polar caps has been interpreted as evidence for glacial flow. However, terrestrial experience suggests that if the Martian north polar cap ever did behave like an active ice sheet, then one would expect that an active layer subglacial till would have formed at its base, and be eventually transported outward towards its margins. On Earth, subglacial till is observed to contain a wide distribution of particle sizes [*Engelhardt et al.,* 1990] and is therefore an interesting candidate source material for the Martian circumpolar dune deposits [B. Kamb, personal communication; 1993]. It should also be noted that *Thomas and Weitz's* [1989] analysis of Viking Orbiter images shows that the source scarps of the polar dune deposits are localized within lowest, oldest regions of the polar layered deposits, which is consistent with the suggestion that the dune deposits may be of subglacial origin.

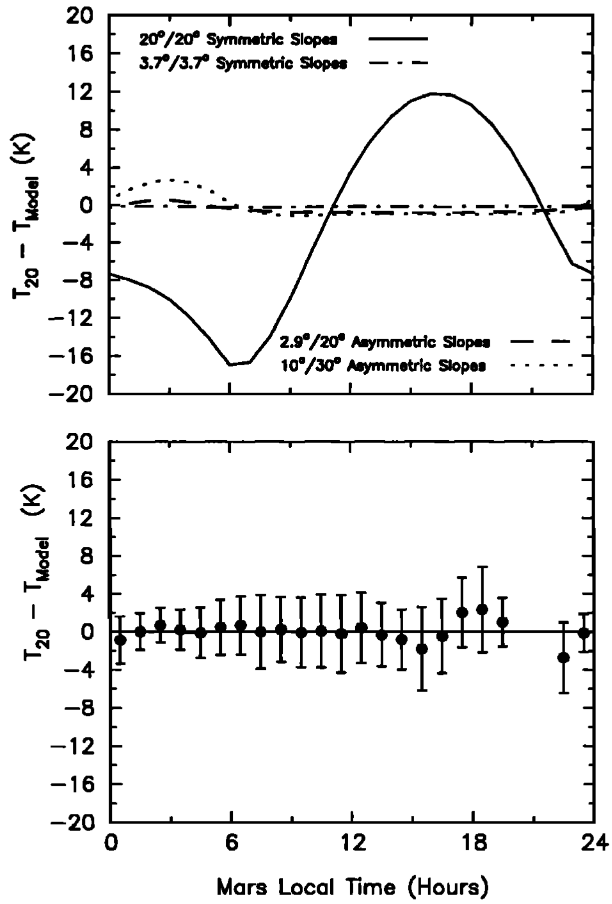

Figure 24. Comparison between models and observations of residual diurnal temperature variability in regions with low apparent thermal inertias that are completely covered by dunes with slope normals oriented in north-east to south-west directions. (Top) Differences between model-calculated IRTM 20-μm channel brightness temperatures and best fit basic thermal model temperatures as a function of Mars local time at 80°N for continuous dune fields with slope normals oriented in north-east to south-west directions. (Bottom) Differences between measured IRTM 20-μm channel brightness temperatures and best fit basic thermal model temperatures for regions with I^* <300 J m^{-2} s$^{-1/2}$ K^{-1} from 78°N to 83°N and 130°W to 205°W. This corresponds to the largest area of complete dune cover in the polar region [*Lancaster and Greeley,* 1990].

Northern Plains

The northern plains regions from 60°N to 80°N contain surface units that are northward extensions of units that have been mapped at lower latitudes. The most distinctive large-scale albedo feature in this region is the dark northern extension of the Acidalia region from 20° to 60°W, which appears to merge with the dark circumpolar dune deposits at 75°N. At 60°N, this dark region has a very high apparent thermal inertia of approximately 550 J m^{-2} $s^{-1/2}$ K^{-1}. By 75°N, its apparent thermal inertia decreases to approximately 350 J m^{-1} $s^{-1/2}$ K^{-1}, with no corresponding increase in best fit albedo or Lambert albedo. This is in sharp contrast to the northern boundary of the high thermal inertia region northward of Utopia Planitia (65°N, 210°W to 310°W), which is marked by a transition from low to high albedo (see Plates 1 and 2). At Martian midlatitudes, dark regions such as Acidalia have been interpreted to be areas that have been stripped of bright, fine-grained material [*Christensen*, 1982; *Greeley et al.*, 1993]. In these areas, most of the remaining terrain is likely to be covered by dark, coarse-grained material that may be analogous to the highest-inertia dark intracrater deposits [*Christensen*, 1982, 1983]. The *Tanaka and Scott* [1987] geologic map indicates the presence of crescentic dunes within the northern Acidalia region at latitudes between 70°N and 80°N. The lower thermal inertia of this area would be consistent with the observed association between lower thermal inertias and dune forms within dark intracrater deposits observed at lower latitudes [*Christensen*, 1983]. However, it should also be pointed out that the one-dimensional atmospheric model results also predict a modest decrease in apparent thermal inertias with latitude during this season for model atmospheres that assume dust optical depths as low as 0.2 (see Figures 12 and 13). Furthermore, if dust opacity decreased with latitude during this season, the model results would predict even lower apparent thermal inertias at higher latitudes. This example helps illustrate the uncertainties inherent in comparing the apparent thermal inertias of widely separated areas without independent information concerning the effects of the Martian atmosphere.

One striking aspect of the apparent thermal inertia map of the north polar region is the complete absence of large low thermal inertia regions. The map shows regions with intermediate apparent thermal inertias extending northward from the Tharsis and Arabia low thermal inertia regions at 90°W to 160°W, and 320°W to 360°W, but by midlatitude standards, these areas cannot be considered low thermal inertia regions in their own right. This absence of low thermal inertia regions poleward of 60°N is somewhat surprising in light of previous work. Both Mariner 9 and Viking observed great dust storms that occurred during the fall and winter seasons in the northern hemisphere. In both cases, the storms were accompanied by elevated polar atmospheric temperatures [*Hanel et al.*, 1972; *Martin and Kieffer*, 1979] due to the transport of heat, and presumably, dust into the north polar region [*Barnes*, 1990]. In fact, the scavenging and precipitation of airborne dust during the polar night by carbon dioxide snow have been proposed as important mechanisms for the removal of dust from the atmosphere during the decay phases of global dust storms [*Pollack et al.*, 1979]. Although there are large uncertainties concerning the total amount of dust that might be deposited in the north polar region over the course of a year, the fact that some dust must get deposited is almost unavoidable. The question of the ultimate fate of the dust has been addressed in a number of studies that consider the origin and evolution of the midlatitude low thermal inertia regions [*Zimbelman and Kieffer*, 1979; *Palluconi and Kieffer*, 1981; *Christensen*, 1982, 1986, 1988]. Clearly, to prevent seasonally deposited dust from accumulating in regions where observations show that surface dust is not present requires the operation of rapid and effective dust removal processes. At midlatitudes, observations of temporal variations in the reflectivities of dark regions have been interpreted as evidence for dust removal processes that operate over seasonal timescales [*Christensen*, 1988]. Therefore the absence of extensive surface dust deposits in the north polar region may not necessarily be evidence that dust is not transported into the north polar region on a seasonal basis. However, the new observations presented in this study indicate that it is safe to conclude that dust is not accumulating in the north polar region under present climatic conditions. The implications of this result for the Martian global dust cycle are discussed more fully in Paper 2.

5. Conclusions

The principal conclusions of this study are listed below by general topic.

North Polar Thermal and Albedo Maps

1. The IRTM instruments observed significant diurnal variations in 20-μm channel brightness temperatures equatorward of 86°N during the northern summer season. By comparing these observed brightness temperature variations to calculated surface temperature variations using the basic thermal model, which ignores the effects of the Martian atmosphere, high-quality maps of the best fit apparent thermal inertia I^*, and best fit apparent albedo A^* of the north polar region can be constructed.

2. The maps of I^* and A^* are well correlated with surface features. At 60°N, the derived thermal inertias and albedos agree with previous thermal inertia and albedo maps. Near the north pole, the derived thermal inertias are in good agreement with previous seasonal thermal inertia estimates based on radiation balance measurements at the top of the atmosphere. Throughout the north polar region, the maps of best fit apparent albedo A^* also agree with maps of measured Lambert albedo A_L which can be constructed independently from IRTM solar channel observations.

3. Differences between IRTM 20-μm channel brightness temperatures, and best fit model-calculated surface temperatures in the north polar region show distinctive patterns of residual diurnal variability that are reminiscent of the "anomalous afternoon cooling" phenomenon observed at lower latitudes.

The Effects of the Atmosphere

1. During the northern summer season, the Martian atmosphere has two major effects on the results presented here. The first is to reduce the amplitudes of diurnal surface temperature variations. The second is to reduce the amplitudes of measured diurnal brightness temperature variations at the top of the atmosphere. The second effect becomes more important as aerosol optical depths at infrared wavelengths increase. Both effects tend to increase the apparent thermal inertia of the surface. Only the first effect has been considered in previous one-dimensional modeling studies.

2. For surfaces with low and intermediate thermal inertias, the Martian atmosphere with no aerosols present nearly doubles apparent thermal inertias during this season. When the effects of dust with a solar-spectrum-averaged optical depth of 0.6 are also included, apparent thermal inertias are nearly quadrupled. Water

ice clouds also increase apparent thermal inertias during this season, but to a lesser degree.

3. Including the effects of the Martian atmosphere results in a ~4 K increase in computed daily averaged surface temperatures during this season for a wide range of assumptions concerning aerosol optical properties and optical depths. During this season, the mild Martian greenhouse effect is increased by the presence of dust and water ice clouds at 60°N and decreased by the presence of these same clouds at the north pole. The effects of aerosols on outgoing infrared radiances at the top of the atmosphere tend to reduce the detectability of the Martian greenhouse effect. The good agreement observed between A^* and A_L in the north polar region during this season is predicted by one-dimensional model calculations.

4. The distinctive patterns of residual diurnal variability observed in the north polar region during this season are also present in model-calculated brightness temperatures. This supports the conclusion of *Haberle and Jakosky* [1991] that these patterns may be largely due to the effects of the atmosphere.

5. Uncertainties in atmospheric temperature structure, aerosol optical properties, and aerosol optical depths make it difficult to compare apparent thermal inertia measurements obtained at different locations and seasons. In regions with low and intermediate inertias, actual surface inertias may be significantly lower than best fit apparent inertias.

North Polar Water Ice Deposits

1. Bright frost deposits on the north residual water ice cap have very high apparent thermal inertias.

2. Detached bright frost deposits surrounding the north residual cap also have very high apparent thermal inertias.

3. Both types of bright frost deposits are interpreted to contain dense, coarse-grained, or solid ice that extends from within 2 mm of the surface to depths of at least 10 cm below the surface. In the core region of the north residual cap, these results are consistent with annual heat balance observations, which suggest that high inertia ice deposits extend to at least 1 m below the surface [*Paige and Ingersoll,* 1985].

4. In the bright core region of the residual cap, estimates of the maximum water vapor holding capacity of the atmosphere based on IRTM surface and atmospheric temperature measurements during this season are consistent with the moderate total column water vapor abundances observed by MAWD.

North Polar Layered Deposits

1. The intermediate-albedo layered deposits surrounding the residual cap have high apparent thermal inertias, and are interpreted to contain coarse-grained or solid ice that extends from within a few millimeters of the surface, to depths of at least 10 cm below the surface.

2. The exposed layered deposits in the north are interpreted to consist of soil-contaminated ice, ice-cemented soil, or ice underlying a thin, darker, ice-free surface layer.

3. In the intermediate-albedo layered deposit regions surrounding the north residual cap, estimates of the maximum water vapor holding capacity of the atmosphere are consistent with the high total column water abundances observed by MAWD. This suggests that the north polar layered deposits could be sources for atmospheric water vapor during this season, and supports the conclusion that they contain near-surface ice.

4. During the summer season, high, saturated water vapor abundances promote the thermal stability of surface, or near-surface ice deposits in the north polar layered terrain regions.

5. Mariner 9 images of the north residual cap obtained in 1972 show much less bright frost coverage than Viking images obtained three Mars years later in 1978. It is suggested that areas in the outer portions of the residual cap were darkened by the deposition of dust, or dust-rich ice during the intense global dust storm of 1971-1972, and were then covered by a thin layer of bright water frost between 1972 and 1978. These observations may be fragmentary evidence for the ongoing formation of layered deposits in the north polar region over interannual timescales.

North Polar Dune Deposits

1. In the north polar region, areas that are completely covered by dark, transverse dune deposits have apparent thermal inertias that are distinctly lower than those of dark intracrater dune deposits at lower latitudes.

2. Arcuate scarp regions within the polar layered deposits that appear to be major sources of polar dune material also appear to have low apparent thermal inertias.

3. The lower apparent thermal inertias of the polar transverse dune deposits may be due to the effects of the atmosphere, or to a real difference in particle properties.

North Polar Plains Regions

1. The northern plains regions from 60°N to 80°N contain thermal inertia and albedo units that are northward extensions of units that have been mapped at lower latitudes.

2. The absence of large, low thermal inertia regions northward of 60°N suggests that atmospheric dust is not accumulating in the north polar region under present climatic conditions.

Acknowledgments. We thank the Viking IRTM team for a acquiring and archiving a superb data set. We thank Bruce Jakosky, Hugh Kieffer, Frank Palluconi and Richard Zurek for many helpful discussions and suggestions, and Robert Haberle and Ken Herkenhoff for thorough and constructive reviews of this manuscript. We also thank Carol Chang for programming assistance, and the JPL Multiple Mission Image Processing Lab for hard copy of the color figures, and Karen McBride-Bei for typesetting this manuscript. This research was supported by the NASA Planetary Geology and Geophysics Program.

References

Barnes, J. R. ,Transport of dust to high northern latitudes in a Martian polar warming, *J. Geophys. Res.*, *95*, 1381-1400, 1990.

Blasius, K. R., J. A. Cutts, and A. D. Howard, Topography and stratigraphy of Martian polar layered deposits, *Icarus*, *50*, 140-160, 1982.

Breed, C. S., M. L. Grolier, and J. F. McCauley, Morphology and distribution of common "sand" dunes on Mars: Comparison with the Earth, *J. Geophys. Res.*, *84*, 8183-8204, 1979.

Budd, W. V., D. Jensen, J. H. I. Leach, I. Smith, and U. Radok, The north polar ice cap of Mars as a steady-state system, *Polarforschung*, *56*, 43-63, 1986.

Capen, C., Return of the Martian Rima Tenius, *Bull. Am. Astron. Soc.*, *12* (3), 726-727, 1980.

Carr, M. H., Periodic climate change on Mars: Review of evidence and effects on distribution of volatiles, *Icarus*, *50*, 129-139, 1982.

Carslaw, H. S., and J. C. Jaeger, *Conduction of Heat in Solids*, 2nd ed., Clarendon Press, Oxford, 1959.

Chandrasekhar, S., *Radiative Transfer*, Dover, Mineola, N.Y., 1960.

Chase, S. C., J. L. Engle, H. W. Eyerly, H. H. Kieffer, F. D. Palluconi, and D. Schofield, Viking infrared thermal mapper, *Appl. Opt*, *17*, 1243-1251, 1978.

Christensen, P. R., Martian dust mantling and surface composition:

Interpretation of thermophysical properties, *J. Geophys. Res.* , *87* , 9985-9998, 1982.

Christensen, P. R., Eolian intercrater deposits on Mars: Physical properties and global distribution, *Icarus*, *56* , 496-518, 1983.

Christensen, P. R., Regional dust deposits on Mars: Physical properties, age, and history, *J. Geophys. Res.*, *91*, 3533-3545, 1986.

Christensen, P. R., Global albedo variations on Mars: Implications for active aeolian transport, deposition, and erosion, *J. Geophys. Res.*, *93*, 7611-7624, 1988.

Christensen, P. R., and R. W. Zurek, Martian north polar hazes and surface ice: Results from the Viking survey/completion mission, *J. Geophys. Res* ., *89*, 4587-4596, 1984.

Clancy, R. T., and S. W. Lee, A new look at dust and clouds in the Mars atmosphere-Analysis of emission-phase-function sequences from global Viking IRTM observations, *Icarus*, *93*, 135-158, 1991.

Clark, R. N., The surface condensates on Mars observed by Viking: Frost layers several tenths of a millimeter thick (abstract), *Lunar Planet. Sci. XI*, 160-161, 1980.

Clifford, S. M., Polar basal melting on Mars, *J. Geophys. Res.*, *92*, 9135-9152, 1987.

Clifford, S. M., and C. J. Bartels, The Mars Thermal Model (MARSTHERM): A Fortran 77 finite difference thermal model designed for general distribution (abstract), *Lunar Planet. Sci.*, XVII, 142-143, 1986.

Crisp, D., S. B. Fels, and M. D. Schwarzkopf, Approximate methods for finding CO_2 15 micron band transmission functions in planetary atmospheres, *J. Geophys. Res.*, *91*, 11,851-11,866, 1986.

Curran, R. J., B. J. Conrath, R. A. Hanel, V. G. Kunde and J. C. Pearl, Mars: Mariner 9 spectroscopic evidence for H_2O ice clouds, *Science*, *182*, 381-383, 1973.

Cutts, J. A., Nature and origin of layered deposits of the Martian polar regions, *J. Geophys. Res.*, *78*, 4231-4249, 1973.

Cutts, J. A., K. R. Blasius, G.A. Briggs, M. H. Carr, R. Greeley, and H. Masursky, North polar region of Mars: Imaging results from Viking 2, *Science*, *194*, 1329-1337, 1976.

Davies, D. W., Effects of dust on the heating of Mars' surface and atmosphere, *J. Geophys. Res.*, *84*, 8289-8293, 1979.

Davies, D. W., The Mars water cycle, *Icarus*, *45*, 398-414, 1981.

Davies, D. W., Water vapor in Mars' arctic: Seasonal and spatial variability, *J. Geophys. Res.*, *87*, 10,253-10,263, 1982.

Dial, A. L., Jr., Geologic map of the Mare Boreum area of Mars, *USGS Misc. Invest. Ser. Map, I-1640* (MC-1), 1984.

Diermendjian, D., *Electromagnetic Scattering of Spherical Polydispersions*, Elsevier, New York, 1969.

Ditteon, R., Daily temperature variations on Mars, *J. Geophys. Res.*, *87*, 10,197-10,214, 1982.

Dzurisin, D., and K. R. Blasius, Topography of the polar layered deposits of Mars, *J. Geophys. Res.*, *80*, 3286-3306, 1975.

Edgett, K. S., and P. R. Christensen, The particle size of Martin Aeolian Dunes, *J. Geophys. Res* , *96*, 22,765-22,776, 1991.

Engelhardt, H., N. Humphrey, B. Kamb, and M. Fahnestock, Physical conditions at the base of a fast moving Antarctic ice stream, *Science*, *248*, 57-59, 1990.

Farmer, C. B., and P. E. Doms, Global seasonal variation of water vapor on Mars and the implications for permafrost, *J. Geophys. Res.*, *84*, 2881-2888, 1979.

Farmer, C. B., D. W. Davies, and D. D. LaPorte, Mars: Northern summer ice cap-water vapor observations from Viking 2, *Science*, *194*, 1339-1341, 1976.

Gierasch, P. J., and R. M. Goody, The effect of dust on the temperature of the Martian atmosphere, *J. Atmos. Sci.*, *29*, 400-402, 1972.

Greeley, R., The case for parna, MECA Workshop on Dust on Mars, *LPI Tech. Rep*. *86-09*, 26-28, 1986.

Greeley. R. and J. D. Iverson, *Wind as a Geological Process on Earth, Mars, Venus, and Titon*, Cambridge University Press, New York, 1985.

Greeley, R., A. Skypek, and J. B. Pollack, Martian aeolian features and deposits: Comparisons with general circulation model results, *J. Geophys. Res.*, *98*, 3183-3196, 1993.

Haberle, R. M., and B. M. Jakosky, Sublimation and transport of water from the north residual polar cap of Mars, *J. Geophys. Res.*, *95*, 1423-1437, 1990.

Haberle, R. M., and B. M. Jakosky, Atmospheric effects on the remote determination of thermal inertia on Mars, *Icarus*, *90*, 187-204, 1991.

Hanel, R., et al., Investigation of the Martian environment by infrared spectroscopy on Mariner 9, *Icarus*, *17*, 423-442, 1972.

Hansen, J. E., and L. D. Travis, Light scattering in planetary atmospheres, *Space Sci. Rev.*, *16*, 527-610, 1974.

Hargraves, R. B., D. W. Collison, R. E. Arvidson, and P. M. Cates, Viking magnetic properties experiment: Extended mission results, *J. Geophys. Res.*, *84*, 8379-8384, 1979.

Herkenhoff, K. E., Dark material in the polar layered deposits on Mars, Workshop on the Martian surface and atmosphere through time, *LPI Tech. Rep.*, *92-02*, 72, 1992.

Herkenhoff, K. E., and B. C. Murray, Color and albedo of the south polar layered deposits on Mars, *J. Geophys. Res.*, *95*, 1343-1358, 1990.

Hofstadter, M. D., and B. C. Murray, Ice sublimation and rheology: Implications for the Martian polar layered deposits, *Icarus*, *84*, 352-361, 1990.

Howard, A. D., J. A. Cutts, and K. R., Blasius, Stratigraphic relationships within the Martian polar cap deposits, *Icarus*, *50*, 161-215, 1982.

Hunt, G. E., Thermal infrared properties of the Martian atmosphere, 4, Prediction of the presence of dust and ice clouds from Viking IRTM spectral measurements, *J. Geophys. Res.*, *84*, 2865-2874, 1979.

Iverson, J. D., and B. R. White, Saltation threshold on Earth, Mars and Venus, *Sedimentology*, *29*, 111-119, 1982.

Jakosky, B. M., and P. R. Christensen, Global duricrust on Mars: Analysis of remote-sensing data, *J. Geophys. Res.*, *91*, 3547-3559, 1986.

Jakosky, B. M., and C. B. Farmer, The seasonal and global behavior of water vapor in the Mars atmosphere: Complete global results of the Viking Atmospheric Water Detector Experiment, *J. Geophys. Res.*, *87*, 2999-3019, 1982.

James, P. B., and L. Martin, Interannual water loss by Mars' north polar cap, *Bull. Amer. Astron. Soc.*, *17*, 735, 1985.

Joseph, J. H., W. J. Wiscombe, and J. A. Weinman, The Delta-Eddington approximation for radiative flux transfer, *J. Atmos. Sci.*, *33*, 2452-2459, 1976.

Kahn, R., The spatial and seasonal distribution of Martin clouds and some meteorological implications, *J. Geophys. Res* , *89*, **6671-6688**, 1984.

Kieffer, H. H., Soil and surface temperatures at the Viking landing sites, *Science* , *194*, 1344-1346, 1976.

Kieffer, H. H., Mars south polar spring and summer temperatures: A residual CO_2 frost, *J. Geophys. Res.*, *84*, 8263-8288, 1979.

Kieffer, H. H., H_2O grain size and amount of dust in Mars' residual north polar cap, *J. Geophys. Res.*, *95*, 1481-1493, 1990.

Kieffer, H. H., S. C. Chase, Jr., T. Z. Martin, E. D. Miner, and F. D. Palluconi, Martian north pole summer temperatures: Dirty water ice, *Science*, *194*, 1341-1344, 1976a.

Kieffer, H. H., P. R. Christensen, T. Z. Martin, E. D. Miner, and F. D. Palluconi, Temperatures of the Martian surface and atmosphere: Viking observation of diurnal and geometric variations, *Science*, *194*, 1346-1351, 1976b.

Kieffer, H. H., T. Z. Martin, A. R. Peterfreund, B. M. Jakosky, E. D. Miner, and F. D. Palluconi, Thermal and albedo mapping of Mars during the Viking primary mission, *J. Geophys. Res.*, *82*, 4249-4291, 1977.

Lancaster, N., and R. Greeley, Sediment volume in the north polar sand sea of Mars, *J. Geophys. Res.*, *95*, 10,921-10,927, 1990.

Leighton, R. B., and B. C. Murray, Behavior of carbon dioxide and other volatiles on Mars, *Science*, *153*, 136-144, 1966.

Leovy, C. B., and Y. Mintz, Numerical simulations of the weather and climate of Mars, *J. Atmos. Sci.*, *26*, 1167-1190, 1969.

Leovy, C. B., and R. W. Zurek, Thermal tides and Martian dust storms: Direct evidence for coupling, *J. Geophys. Res.*, *84*, 2956-2968, 1979.

Malin, M. C., Density of Martian north polar layered deposits:

Implications for composition, *Geophys. Res. Lett.*, *13*, 444-447, 1986.

Martin, T. Z., and H. H. Kieffer, Thermal infrared properties of the Martian atmosphere , 2, The 15 micron band measurements, *J. Geophys. Res.*, *84*, 2843-2852, 1979.

Murray, B. C., L. A. Soderblom, J. A. Cutts, R. P. Sharp, D. J. Milton, and R. B. Leighton, Geologic framework of the south polar region of Mars, *Icarus*, *17*, 328-345, 1972.

Paige, D. A., The annual heat balance of the Martian polar caps, Ph.D. dissertation, Calif. Inst. of Technol. Pasadena, 1985.

Paige, D. A., The thermal stability of near-surface ground ice on Mars, *Nature*, *356*, 43-45, 1992.

Paige, D. A., and A. P. Ingersoll, Annual heat balance of Martian polar caps: Viking observations, *Science*, *228*, 1160-1168, 1985.

Paige, D. A., and K. D. Keegan, Thermal and albedo mapping of the polar regions of Mars using Viking thermal mapper observations, 2, South polar region, *J. Geophys. Res.*, this issue.

Palluconi, F. D., and H. H. Kieffer, Thermal inertia mapping of Mars from 60°S to 60°N, *Icarus*, *45*, 415-426, 1981.

Plaut, J. J., R. Kahn, E. A. Guiness, and R. E. Arvidson, Accumulation of sedimentary debris in the south polar region of Mars and implications for climate history, *Icarus*, *75*, 357-377, 1988.

Pleskot, L. K., and E. D. Miner, Time variability of Martian bolometric albedo, *Icarus*, *50*, 259-287, 1982.

Pollack, J. B., O. B. Toon, and B. N. Khare, Optical properties of some terrestrial rocks and glasses, *Icarus*, *19*, 372-389, 1973.

Pollack, J. B., D. Colburn, R. Kahn, J. Hunter, W. Van Camp, C. E. Carlston, and M. R. Wolf, Properties of aerosols in the Martian atmosphere, as inferred from Viking lander imaging data, *J. Geophys. Res.*, *82*, 4479-4496, 1977.

Pollack, J. B., D. S. Colburn, F. M. Flasar, R. Kahn, C. E. Carlston, and D. Pidek, Properties and effects of dust particles suspended in the Martian atmosphere, *J. Geophys. Res.*, *84*, 2929-2945, 1979.

Pollack, J. B., C. B. Leovy, P. W. Greiman, and Y. Mintz, A Martian general circulation experiment with large topography, *J. Atmos. Sci.*, *38*, 3-29, 1981.

Santee, M. L., The thermal structure, dust loading and meridional transport in the Martian atmosphere during late southern summer, Ph.D. thesis, Calif. Inst. of Technol., Pasadena, 1992.

Santee, M. L., and D. Crisp, The thermal structure and dust loading of the Martian atmosphere during late southern summer: Mariner 9 revisited, *J. Geophys. Res.*, *98*, 3261-3279, 1993.

Saunders, R. S., and D. T. Blewett, Mars north polar dunes: Possible formation from low density sediment aggregates, *Astron. Vestn.*, *21*, 181-188, 1987.

Saunders, R. S., F. P. Fanale, T. J. Parker, J. B. Stephens, and S. Sutton, Properties of filamentary sublimation residues from dispersion of clay and ice, *Icarus*, *66*, 94-104, 1986.

Schaaf, J. W., and D. Williams, Optical constants of ice in the infrared, *J. Opt. Soc. Am.*, *63*, 726-732, 1973.

Tanaka, K. L., and D. H. Scott, Geologic map of the polar regions of Mars, Atlas of Mars, 1:15,000,000, *Geol. Ser.*, *I-1802-C*, U.S. Geol. Surv., Reston, Va., 1987.

Thomas, P. J., and J. Veverka, Red/violet contrast reversal on Mars: Significance for aeolian sediments, *Icarus*, *66*, 39-55, 1986.

Thomas, P., and C. Weitz, Sand dune materials and polar layered deposits on Mars, *Icarus*, *81*, 185-215, 1989.

Thomas, P., K. E. Herkenhoff, A. D. Howard, B. C. Murray, and S. L. Squyres, Polar deposits of Mars, in *Mars*, University of Arizona Press, Tuscon, 1992.

Toon, O. B., J. B. Pollack, and C. Sagan, Physical properties of the particles composing the Martian dust storm of 1971-2, *Icarus*, *30*, 663-696, 1977.

Toon, O. B., J. B. Pollack, W. Ward, J. A. Burns, and K. Bilski, The astronomical theory of climatic change on Mars, *Icarus*, *44*, 552-607, 1980.

Tsoar, H., R. Greeley, and A. R. Peterfreund, Mars: The north polar sand sea and related wind patterns, *J. Geophys. Res.*, *84*, 8167-8180, 1979.

U.S. Geological Survey, Mission to Mars: Digital Color Mosaics CD ROM, vol. 8: Vastitas Borealis Region, Reston, Va., 1993.

Ward, W. R., Climatic variations on Mars, 1, Astronomical theory of insolation, *J. Geophys. Res.*, *79*, 3375-3386, 1974.

Ward, W. R., B. C. Murray, and M. C. Malin, Climatic variations on Mars, 2, Evolution of carbon dioxide atmosphere and polar caps, *J. Geophys. Res.*, *79*, 3387-3395, 1974.

Wechsler, A. E., and P. E. Glaser, Pressure effects on postulated lunar materials, *Icarus*, *4*, 335-352, 1965.

White, B. R., Soil transport by winds on Mars, *J. Geophys. Res.*, *84*, 4643-4651, 1979.

Wiscomb, W. J., and S. G. Warren, A model for the spectral albedo of snow, I, Pure snow, *J. Atmos. Sci.*, *37*, 2712-2733, 1980.

Wood, S. E., and D. A. Paige, Modeling the Martian seasonal CO_2 cycle, 1, Fitting the Viking lander pressure curves, *Icarus*, *99*, 1-14, 1992.

Zimbelman, J. R., and H. H. Kieffer, Thermal mapping the northern equatorial and temperate latitudes of Mars, *J. Geophys. Res.*, *84*, 8239-8251, 1979.

J. E. Bachman, K. D. Keegan, and D. A. Paige, Department of Earth and Space Sciences, University of California, Los Angeles, Los Angeles, CA 90024.

(Received June 23, 1992; revised November 2, 1993; accepted December 3, 1993.)